Earth Syst. Sci. Data, 18, 8591–8615, 2026
https://doi.org/10.5194/essd-18-8591-2026
© Author(s) 2026. This work is distributed under
the Creative Commons Attribution 4.0 License.

Open Access Earth System Science Data

A multi-decadal dataset of surface damage on Antarctic ice shelves (1999–2024)

Leyue Tang[1,2], Jonathan L. Bamber[2,3], Tian Li[2], and Gang Qiao[1]

[1]Center for Spatial Information Science and Sustainable Development Applications, College of Surveying and Geo-Informatics, Tongji University, Shanghai 200092, China
[2]Bristol Glaciology Centre, School of Geographical Sciences, University of Bristol, Bristol, BS8 1SS, UK
[3]Institute for Advanced Study, Technical University of Munich, 85748 Garching, Germany

Correspondence: Gang Qiao (qiaogang@tongji.edu.cn)

Received: 30 May 2026 – Discussion started: 29 June 2026
Revised: 6 November 2026 – Accepted: 14 November 2026 – Published: 20 November 2026

Abstract. Many Antarctic ice shelves have undergone accelerated thinning and retreat in recent decades, weakening their buttressing effect on grounded ice and increasing the risk of further sea-level rise. Surface damage, including crevasses, rifts and heavily fractured areas, is an important indicator of ice shelf structural integrity, but there is limited understanding of its long-term evolution across Antarctic ice shelves. Here we present a new surface damage dataset for nine representative Antarctic ice shelves, derived from Landsat optical imagery covering the period 1999–2024. These ice shelves include Amery, Brunt, Crosson, Dotson, Holmes, Pine Island, Scar Inlet, Thwaites and Totten, and encompass a range of change behaviours from relatively stable to rapidly changing systems. A deep-learning image segmentation model was trained on a manually annotated dataset from diverse Antarctic ice shelves to automatically map surface damage. To extend the usable record, Landsat 7 scan-line-corrector-off imagery was restored using a diffusion-model-based framework fine-tuned for Antarctic imagery. The final dataset contains 170 surface damage maps at 30 m resolution, each representing a single ice shelf for a specific year. Temporal coverage varies among ice shelves owing to differences in the availability of usable imagery. Evaluation on two independent test sets indicates that the model generalizes well across spatially distinct and cross-sensor settings. The dataset demonstrates good multi-temporal consistency, supporting its use for time-series analysis. Among the nine ice shelves, Pine Island, Thwaites and Scar Inlet show the most pronounced surface damage changes during the study period. Compared with existing studies, this dataset provides improved temporal continuity over multi-decadal timescales at substantially finer spatial resolution, offering new insights into the long-term evolution of Antarctic ice shelves and contributing to a better understanding of ice shelf instability. The dataset is publicly available at https://doi.org/10.5281/zenodo.20425951 (Tang et al., 2026a).

1 Introduction

As the largest reservoir of land ice on Earth, the Antarctic Ice Sheet (AIS) represents the greatest potential contributor to global sea-level rise and the dominant source of uncertainty in future sea-level-rise projections (Fricker et al., 2025). Between 1992 and 2020, the AIS lost 2671 ± 530 Gt of ice, contributing 7.4 ± 1.5 mm to global sea-level rise (Otosaka et al., 2023). The floating ice shelves provide important buttressing to the grounded ice sheet. The thinning and retreat of ice shelves can weaken this buttressing effect, promoting faster inland ice flow and increased ice discharge into the ocean, and thereby increasing the future contribution of the AIS to global sea-level rise (Miles and Bingham, 2024; Bassis et al., 2024). Antarctic ice shelves have undergone substantial changes in recent decades. Between 1997 and 2021, the total area of Antarctic ice shelves decreased by $36\,701 \pm 1465$ km^2 (1.9 %), mainly driven by major calving events (Greene et al., 2022). Widespread thinning over the same period has fur-

ther contributed to Antarctic ice-shelf mass loss (Davison et al., 2023). Continuous monitoring of Antarctic ice shelves is therefore critical for understanding their stability and assessing their future evolution.

Surface damage is an important indicator of ice shelf structural weakening and changes in rheological properties (Colgan et al., 2016). It can weaken ice shelf structural integrity, thereby promoting calving and the associated ice-front retreat (Borstad et al., 2012). Surface damage on ice shelves includes crevasses, rifts and heavily fractured areas, such as intensely fractured zones within shear margins. Damage development is linked to enhanced shear, ice flow acceleration, increased strain rates and ice shelf thinning, with these interactions being climate-sensitive and becoming more pronounced in a warming climate (Izeboud et al., 2025). In addition, oceanic and atmospheric forcing can also contribute to damage development (Massom et al., 2018; Francis et al., 2021; Marsh et al., 2025). Studies have shown that damage evolution is closely associated with the disintegration and structural weakening of several major ice shelves, such as Larsen B (Glasser and Scambos, 2008), Brunt (Marsh et al., 2025), Amery (Walker et al., 2021), Pine Island (Lhermitte et al., 2020; Surawy-Stepney et al., 2023b) and Thwaites (Benn et al., 2022; Surawy-Stepney et al., 2023a).

Given the critical role of surface damage in ice shelf stability, long-term and large-scale monitoring of its evolution is essential for understanding ice shelf change and reducing uncertainty in future projections. Remote sensing imagery provides an important data source for such monitoring. However, publicly available surface damage products for Antarctic ice shelves remain limited (Table 1). Lai et al. (2020) produced a single-temporal surface damage map of Antarctic ice shelves for 2009 based on MODIS Mosaic of Antarctica (MOA) (Scambos et al., 2007) imagery at a spatial resolution of 125 m. Also based on MOA imagery, Pang et al. (2023) generated products for 2004, 2009 and 2014 at the same spatial resolution. Surawy-Stepney et al. (2023b) released a single-temporal product for June 2021 based on Sentinel-1 SAR imagery, at a spatial resolution of 100 m. Izeboud et al. (2025) also used SAR imagery and released products for 1997, 2000 and 2021 at a spatial resolution of 1000 m, as well as annual products for 2015–2021 at a spatial resolution of 400 m. This product represents the longest temporal coverage among existing surface damage products. The results revealed that the area of surface damage generally decreased across Antarctic ice shelves between 1997 and 2021, mainly because damaged areas were lost through calving, and that damage development was strongly correlated with ice shelf area changes (Izeboud et al., 2025). However, this product is still limited by its relatively coarse spatial resolution, and continuous annual temporal coverage is only available from 2015 onwards, leaving the earlier period from 1997 through 2014 represented by only three snapshot years. More broadly, existing studies have primarily relied on MOA and SAR imagery for large-scale damage mapping. Because MOA imagery is only available for 2004, 2009 and 2014, and stable, frequent SAR acquisitions only became available after the launch of Sentinel-1 in 2014, early temporal coverage in existing products is generally sparse and discontinuous. Overall, existing openly available products are limited in both spatial and temporal resolution, constraining detailed and continuous monitoring and analysis of rapidly changing ice shelves over multi-decadal time scales.

Generating long-term, high-resolution surface damage datasets over large spatial scales requires feature-extraction methods that are both accurate and scalable. Early studies mainly relied on manual visual interpretation of remote sensing imagery to map damage features (Hulbe et al., 2010). With the development of image processing techniques, some studies have used automatic methods such as edge detection for damage extraction (Lv et al., 2022). Izeboud and Lhermitte (2023) developed an improved image processing algorithm, the Normalised Radon Transform Detection (NeRD), and applied it to Synthetic Aperture Radar (SAR) imagery to map surface damage on Antarctic ice shelves (Izeboud et al., 2025). However, such conventional image processing methods generally rely on empirical parameter settings and may require case-specific adjustment across different regions. Deep-learning (DL) techniques, by contrast, have shown strong potential for learning representative features from remote sensing imagery automatically and efficiently (Li et al., 2024b), making them well suited to large-scale, long-term damage mapping. Related studies have applied DL methods to damage mapping using optical imagery (Lai et al., 2020; Pang et al., 2023; Zheng et al., 2024; Li et al., 2024a, 2025b), SAR imagery (Zhao et al., 2022; Surawy-Stepney et al., 2023a, b), and combined optical and SAR imagery (Huang et al., 2025). In addition to image-based mapping, altimetry data and digital elevation models (DEMs) have also been used for the identification and characterization of surface damage (Wang et al., 2021; Herzfeld et al., 2021; Li et al., 2021, 2025a; Huang et al., 2024; Pang et al., 2026; Xu et al., 2026). However, given their limitations in spatiotemporal resolution and coverage, image-based mapping remains better suited to multi-decadal, large-scale and continuous monitoring of surface damage evolution.

To address the limitations of existing products, we apply a deep-learning method to Landsat 7/8/9 optical imagery to produce a high-resolution surface damage dataset for nine representative Antarctic ice shelves at a spatial resolution of 30 m, with multi-decadal temporal coverage from 1999 through 2024. Landsat optical imagery provides a long-term observational record that helps fill the early temporal gaps in existing SAR-based products, while also enabling higher-resolution mapping of surface damage. These nine ice shelves represent three contrasting glaciological settings and damage evolution patterns (Fig. 2). The first group comprises Pine Island, Thwaites, Crosson and Dotson in the Amundsen Sea sector, where pronounced thinning, retreat and surface damage development have been widely documented (Lilien

Table 1. Summary of publicly available surface damage datasets for Antarctic ice shelves (DL: deep learning, NeRD: Normalised Radon Transform Detection).

Study	Method	Sensor	Spatial resolution	Time span	Temporal resolution
Lai et al. (2020)	DL	Optical	125 m	2009	Single epoch
Pang et al. (2023)	DL	Optical	125 m	2004, 2009, 2014	3 epochs
Surawy-Stepney et al. (2023b)	DL	SAR	100 m	2021	Single epoch
Izeboud et al. (2025)	NeRD	SAR	400 m 1000 m	2015–2021 1997, 2000, 2021	Annual 3 epochs
This study	DL	Optical	30 m	1999–2024	Annual

et al., 2018; Lhermitte et al., 2020; Joughin et al., 2021; Wang et al., 2025). The second group includes Scar Inlet on the Antarctic Peninsula and Brunt in East Antarctica. Following the major collapse of Larsen B Ice Shelf in 2002, its remnant, now known as Scar Inlet Ice Shelf, has continued to undergo further damage development, while Brunt is characterised by rift formation and recent calving events (King et al., 2018; Qiao et al., 2020; Surawy-Stepney et al., 2024; Morris et al., 2025). The third group consists of Amery, Totten and Holmes in East Antarctica, including ice shelves with relatively stable conditions as well as those experiencing instabilities such as recent unpinning and grounding line retreat (Greene et al., 2022; Zhu et al., 2023; Miles and Bingham, 2024; Miles et al., 2025; Jin et al., 2025). Together, these ice shelves provide a basis for investigating long-term surface damage evolution across contrasting ice shelf settings. Following the failure of the Landsat 7 scan-line corrector (SLC) in 2003, subsequently acquired imagery, referred to as SLC-off imagery, contains systematic data gaps that can obscure surface damage features. To extend the usable record, Landsat 7 SLC-off imagery acquired during 2003–2013 was therefore restored using a specifically designed diffusion-model-based framework (Sect. 2.2) prior to damage mapping. The dataset contains 170 surface damage maps, each representing a single ice shelf for a specific year, with temporal coverage shown in Fig. 3.

2 Data and methods

2.1 Study regions and source imagery

2.1.1 Regions of interest

During dataset generation, each ice shelf is processed separately as an independent object. To ensure sufficient coverage of the study area throughout the study period, this study determines a region of interest (ROI) for each ice shelf based on the MEaSUREs ice shelf extent product (Mouginot et al., 2017), combined with the maximum spatial extent of each ice shelf during the study period and with appropriate outward expansion (Fig. 4). The resulting ROI is used as the image download extent and is designed to include, as completely as possible, areas of frontal change and regions near the grounding line.

2.1.2 Data sources

To generate surface damage maps of Antarctic ice shelves for 1999–2024, this study uses optical multispectral imagery acquired by Landsat 7 (EROS Center, 2020a), Landsat 8 and Landsat 9 (EROS Center, 2020b), and selects the red, green and blue (RGB) bands for processing. The imagery has a spatial resolution of 30 m (Table 2). Imagery acquired between December 1999 and March 2013 was from Landsat 7, while imagery acquired from April 2013 onwards was mainly from Landsat 8, with some imagery acquired after October 2021 from Landsat 9. Due to polar night conditions in Antarctica, the acquisition window for usable optical imagery is limited to the sunlit season, from November to March of the following year, broadly corresponding to the austral summer. In the following sections, imagery for a given year refers to imagery acquired during the sunlit season starting in that calendar year.

2.1.3 Image selection and acquisition

The imagery used for dataset generation was primarily acquired through the Google Earth Engine (GEE) platform. Landsat imagery was obtained from the Landsat Collection 2 calibrated top-of-atmosphere (TOA) reflectance dataset. Landsat imagery within the ROI of each ice shelf was screened separately for each sunlit season (Fig. 1a). As cloud cover is one of the main limiting factors in the use of optical imagery in Antarctica, candidate images were first screened using a threshold of 80 % based on the "cloud_cover" property in the image metadata. This threshold was set to retain as many potentially usable images as possible. For imagery that passed this initial screening, cloud and cloud-shadow pixels were then masked using the QA_PIXEL band provided with the Landsat products in GEE. If multiple images

Table 2. Data sources used for dataset generation.

Satellite	Time span	Bands	Resolution
Landsat 7	Dec 1999–Mar 2013	Red, Green, Blue (3, 2, 1)	30 m
Landsat 8	Apr 2013–Mar 2025	Red, Green, Blue (4, 3, 2)	30 m
Landsat 9	Oct 2021–Mar 2025	Red, Green, Blue (4, 3, 2)	30 m

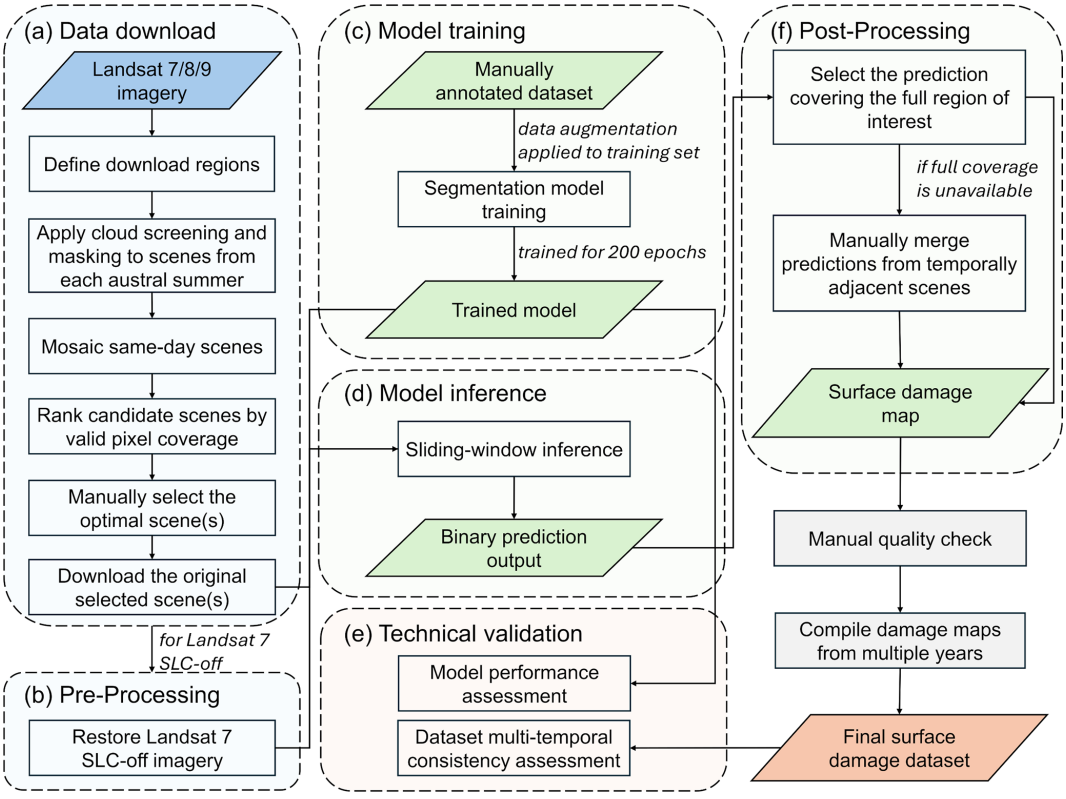


Figure 1. Workflow for surface damage mapping. Each ice shelf is processed separately. **(a)** Data download. **(b)** Pre-processing for Landsat 7 SLC-off imagery. **(c)** Model training. **(d)** Model inference. **(e)** Technical validation. **(f)** Post-processing of the dataset.

were available for the same day, they were mosaicked into a single daily image (hereafter referred to as a scene). The scenes were then ranked according to the proportion of valid (i.e., cloud-free) pixels, and further manually screened based on the same criteria. Priority was given to cloud-free scenes that fully covered the ROI. If such scenes were unavailable, scenes with a relatively high proportion of valid coverage over the ROI were selected. For the final selected scenes, the original imagery without cloud masking was downloaded for subsequent dataset generation. This procedure was repeated for each ice shelf and each year from 1999 through 2024.

The downloaded imagery was exported as GeoTIFF files in unsigned 8-bit (UInt8) format. The export coordinate system was the WGS 84/Antarctic Polar Stereographic projection (EPSG:3031), and the value range of each band was 0–255. For 2023 and 2024, some imagery exported from GEE contained large data gaps, possibly caused by anomalies during the export process. These images were instead downloaded from the USGS website (https://earthexplorer.usgs.gov/, last access: 18 November 2026) as Landsat 8 Collection 2 Level-1 products. QGIS was then used for band combination, ROI clipping and data format conversion. The final output imagery was consistent with the GEE-exported imagery in format, resolution, projected coordinate system, value range and spatial extent. Through this selection and acquisition procedure, candidate scenes for damage mapping were determined for each ice shelf in each available year.

2.2 Pre-processing of Landsat 7 SLC-off imagery

The Landsat 7 satellite experienced a permanent failure of the scan-line corrector in May 2003. As a result, all imagery acquired thereafter contains stripe-shaped data gaps and is referred to as SLC-off imagery. These gaps interfere with the extraction of surface damage on ice shelves and thus affect

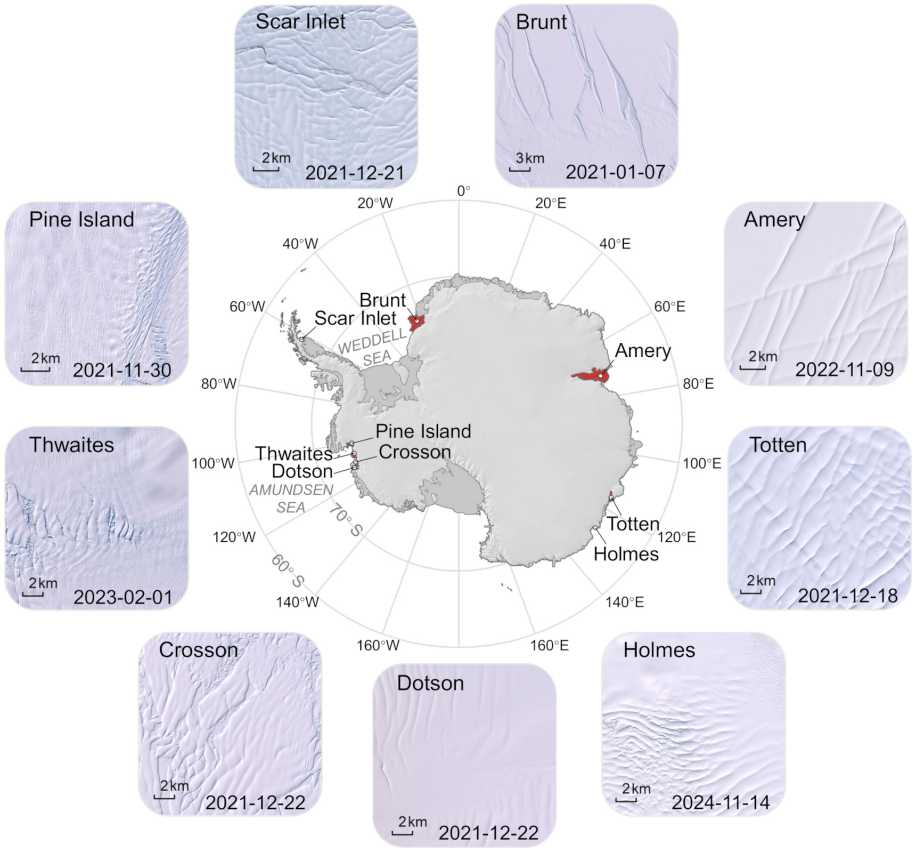


Figure 2. Spatial distribution of the nine ice shelves included in this dataset in Antarctica, with the background imagery and boundaries from Bedmap2 (Fretwell et al., 2013; Fretwell et al., 2022). Surrounding panels show representative examples of surface damage on each ice shelf, with annotations indicating the acquisition dates of the Landsat imagery.

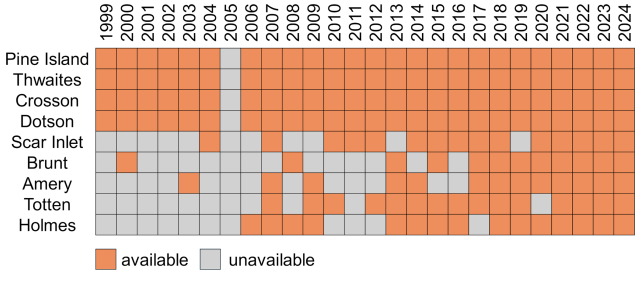


Figure 3. Temporal coverage of this dataset for each ice shelf. Orange cells denote that a surface damage map is available for that ice shelf in a given year, whereas grey cells denote that no surface damage map is available.

the mapping results. To reduce their impact, this study applies the DiffGF framework (Tang et al., 2026b) to restore the Landsat 7 SLC-off imagery used in this study (Fig. 1b).

DiffGF is a non-reference two-stage restoration framework designed for restoring data gaps in Antarctic Landsat 7 SLC-off imagery. The method first exploits the generative capability of a diffusion model to restore missing regions using only a single SLC-off image and performs the diffusion process in latent space to improve computational efficiency. It then further enhances the consistency between restored and known regions through a mask-guided harmonization process in pixel space, thereby producing the final restoration result. This framework is suitable for Antarctic ice shelves that experience rapid changes in surface conditions and for which effective reference imagery is difficult to obtain. Under such conditions, traditional reference-based restoration methods are often difficult to apply.

The DiffGF framework was trained on SLCANT (Tang et al., 2026b), a dataset consisting of 3139 simulated SLC-off images of 256×256 pixels. These simulated images were generated by applying real Landsat 7 SLC-off masks to complete Landsat 8 images, with the corresponding complete Landsat 8 images serving as ground truth. The source images were collected from 10 representative regions in Antarctica, covering a range of typical Antarctic surface features, including ice- and snow-covered surfaces, coastlines, bare rock, different types of surface damage features, blue ice and melt ponds. Landsat 7 SLC-off imagery is then restored using the trained DiffGF framework, and the restored images are used for damage mapping in this study. Further details

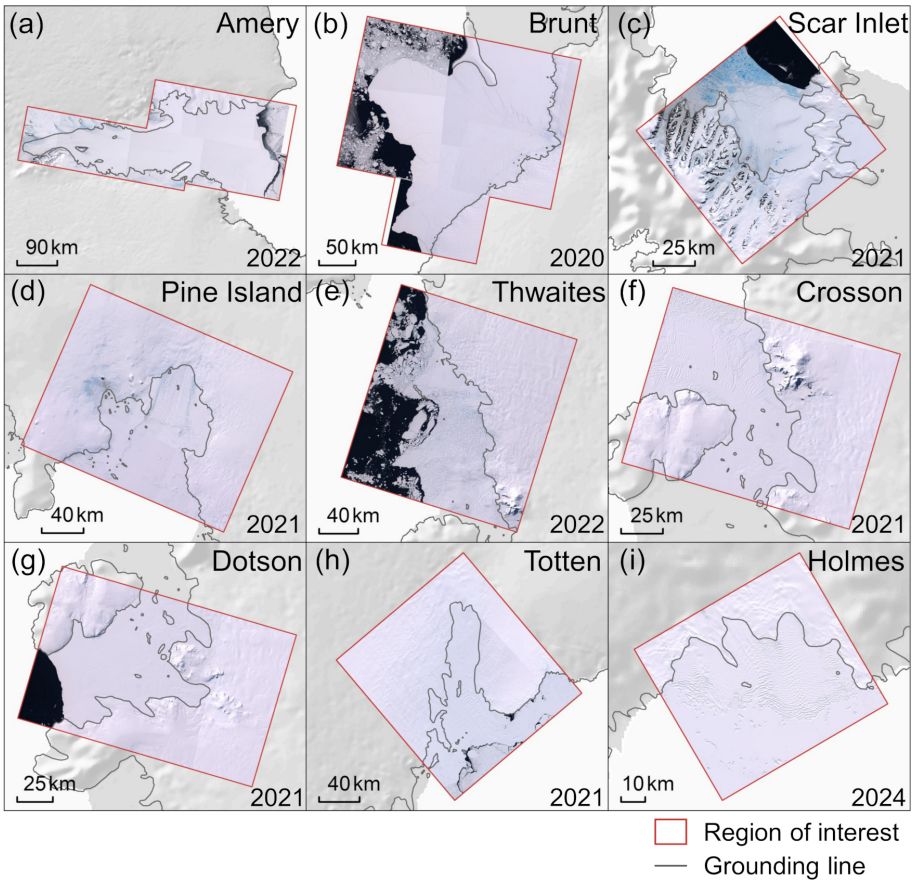


Figure 4. Regions of interest (ROIs) used for imagery download and corresponding Landsat imagery for **(a)** Amery, **(b)** Brunt, **(c)** Scar Inlet, **(d)** Pine Island, **(e)** Thwaites, **(f)** Crosson, **(g)** Dotson, **(h)** Totten, and **(i)** Holmes Ice Shelves. The grounding lines are from Mouginot et al. (2017), and the annotated years indicate the sunlit seasons during which the Landsat imagery was acquired.

of the simulated training dataset and the training process of DiffGF are provided in Tang et al. (2026b). The restoration performance of DiffGF was also evaluated in Tang et al. (2026b) using metrics including Peak Signal-to-Noise Ratio (PSNR) (Horé and Ziou, 2010), Universal Image Quality Index (UIQI) (Wang and Bovik, 2002), Structural Similarity Index Measure (SSIM) (Wang et al., 2004), Learned Perceptual Image Patch Similarity (LPIPS) (Zhang et al., 2018), root mean square error (RMSE) and correlation coefficient (CC).

2.3 Surface damage mapping with deep learning

2.3.1 Manually annotated dataset

To train and validate a deep-learning image segmentation model, a manually annotated surface damage dataset was created in this study. The imagery used for dataset construction was selected from cloud-free Landsat 8 RGB imagery acquired over diverse ice shelves (Fig. S1 in the Supplement), to capture a broad range of surface damage features and help improve model robustness and transferability. All imagery was acquired during the sunlit season of 2020 (Table S1 in the Supplement).

To improve annotation quality and confidence, the annotation process was assisted by multi-source remote sensing data, including Sentinel-1 SAR imagery and ICESat-2 laser altimetry data acquired at a similar time. This strategy allowed surface damage to be interpreted jointly from optical appearance, SAR backscatter characteristics, and surface elevation, helping to reduce interpretation uncertainty and subjectivity. Specifically, for each Landsat 8 image used for annotation, Sentinel-1 SAR Interferometric Wide Swath (IW) Ground Range Detected (GRD) data covering the same region and with the temporally closest available acquisition date were selected. The acquisition-date difference between the Landsat 8 and selected Sentinel-1 images ranged from 0 to 3 d. The Sentinel-1 data were downloaded and processed in SNAP through a standard workflow, including thermal noise removal, radiometric calibration, speckle filtering, and terrain correction using the REMA DEM (Howat et al., 2019, 2022), to derive geocoded backscatter imagery. ICESat-2 ATL06 data acquired within a 91 d window centred on each

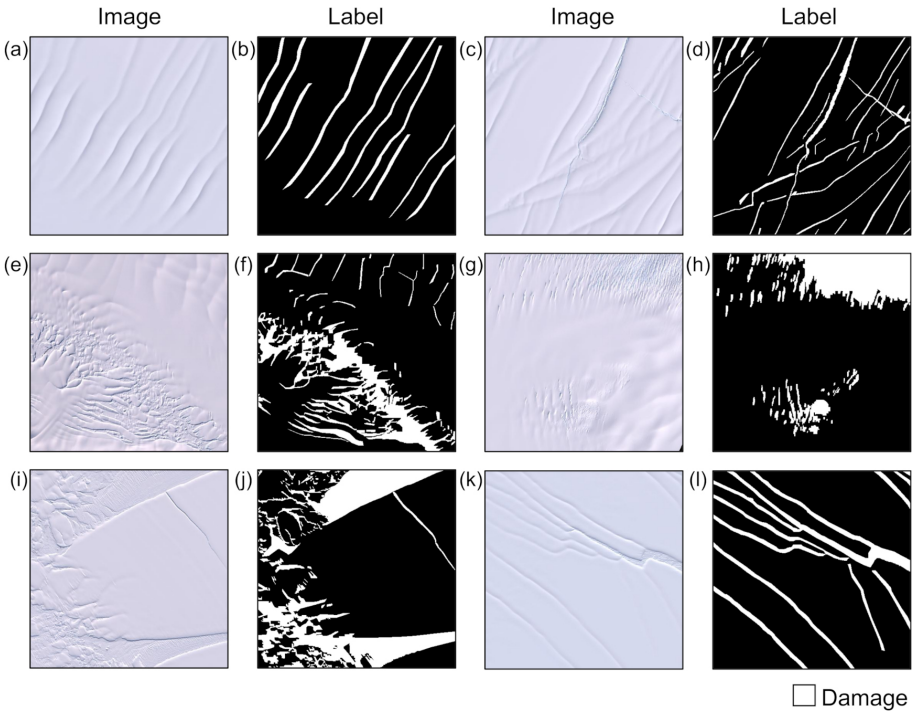


Figure 5. Examples from the manually annotated surface damage dataset, showing image samples and their corresponding labels. Image samples are from Amery Ice Shelf (**a, c**, 6 January 2021), Crosson Ice Shelf (**e**, 31 January 2021), Pine Island Ice Shelf (**g**, 12 December 2020), Ronne Ice Shelf (**i**, 15 January 2021) and Larsen C Ice Shelf (**k**, 29 Decembert 2020), with **(b)**, **(d)**, **(f)**, **(h)**, **(j)** and **(l)** showing the corresponding annotated labels.

Landsat 8 acquisition date (45 days before to 45 d after) were used. This window corresponds to one ICESat-2 repeat cycle. The data were downloaded and processed following Wang et al. (2021) to provide additional surface elevation information for identifying surface damage.

The manually annotated dataset includes multiple manifestations of surface damage, from individual crevasses and rifts to densely fractured areas (Fig. 5). These features were annotated as a single damage class. Surface damage was identified in the Landsat imagery based on distinct linear or curvilinear surface discontinuities and densely fractured areas characterized by clearly disrupted surface patterns. In contrast, general surface roughness and other gradual variations in surface appearance were not labelled as damage in the absence of distinct surface discontinuities or clearly disrupted patterns. The final annotated dataset contains 276 images of 512×512 pixels.

2.3.2 Segmentation model

We used SegFormer (Xie et al., 2021) as the image segmentation model in this study. SegFormer is a Transformer-based model with the ability to capture wider spatial context, which is suitable for identifying surface damage with heterogeneous spatial patterns and varying morphology. The model output is a binary segmentation result with two classes: damage and background (Fig. 6).

SegFormer-B2 was adopted in this study. The model was implemented in Python with PyTorch and the Transformers library. Training was conducted on an NVIDIA A100 GPU in a shared high-performance computing environment with non-exclusive GPU allocation.

To further assess its suitability for this task, SegFormer-B2 was compared with U-Net (Ronneberger et al., 2015) using a ResNet-34 encoder and DeepLabV3+ (Chen et al., 2018) using a ResNet-50 encoder under the same training strategy. SegFormer achieved the best overall performance (Table S2) and was therefore selected for surface damage mapping.

2.3.3 Training strategy

The manually annotated damage dataset is used for model training and validation, with 224 images (80 %) used as the training set and 52 images (20 %) used as the validation set. Images from each region are randomly allocated to the training and validation sets to ensure that both subsets capture a representative range of surface damage characteristics. No spatial overlap exists between any images. Geographic generalizability is further evaluated using test data from ice shelves not represented in either the training or validation set (Sects. 2.5.1 and 3.2.2). To address the class imbalance be-

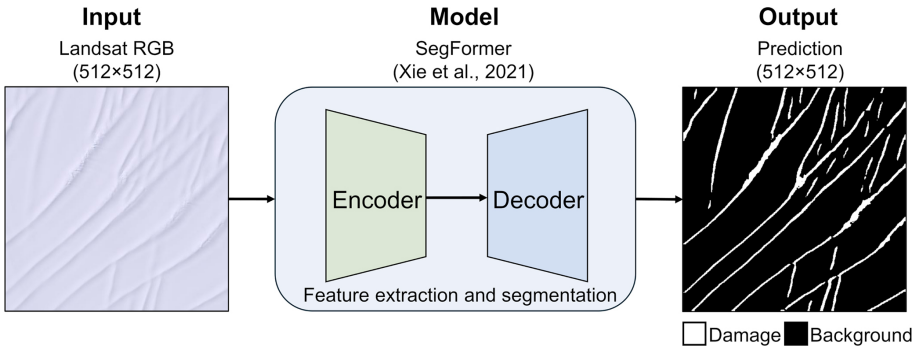


Figure 6. Schematic overview of SegFormer-based surface damage segmentation.

tween damage and background in the annotations, this study adopts a composite loss function combining binary cross-entropy loss (Eq. 1) and Dice loss (Eq. 2), referred to as BCED (Eq. 3), for model training:

$$\mathcal{L}_{\mathrm{BCE}} = -\frac{1}{N}\sum_{i=1}^{N}\left[y_i \log(p_i) + (1-y_i)\log(1-p_i)\right] \tag{1}$$

$$\mathcal{L}_{\mathrm{Dice}} = 1 - \frac{2\sum_{i=1}^{N} y_i\, p_i + \epsilon}{\sum_{i=1}^{N} y_i + \sum_{i=1}^{N} p_i + \epsilon} \tag{2}$$

$$\mathcal{L}_{\mathrm{BCED}} = \mathcal{L}_{\mathrm{BCE}} + \mathcal{L}_{\mathrm{Dice}} \tag{3}$$

where N denotes the total number of pixels, y_i is the ground-truth label of the ith pixel, p_i is the probability predicted by the model that the pixel belongs to the damage class, and ϵ is a constant smoothing term.

The training hyperparameters were selected based on preliminary experiments, model convergence behaviour and computational constraints. The learning-rate schedule and number of epochs were determined according to model convergence, while the batch size was selected considering GPU memory availability. During model training, the batch size is set to 8 and the model is trained for 200 epochs using the AdamW optimizer. For the first 20 epochs, a linear warm-up strategy is adopted to increase the learning rate from 1×10^{-5} to 1×10^{-4}. In the subsequent 80 epochs, a cosine annealing strategy is used to smoothly decay the learning rate to 5×10^{-5}. During the final 100 epochs, this learning rate is maintained for final fine-tuning to promote stable model convergence. During training, all training images were subject to a random augmentation procedure comprising rotation between -45 and 45° and brightness adjustment within ±25 %. Rotation was applied to each training sample, whereas brightness adjustment was applied with a probability of 50 %. These augmentations were used to increase sample diversity and improve model robustness and generalization ability. The model checkpoint with the best performance on the validation set was selected as the final model. The selected checkpoint corresponded to epoch 190.

2.4 Post-processing

2.4.1 Generation of full-ROI damage maps

The trained image segmentation model is used to map damage from the selected scenes. To generate damage maps covering the full ROI, further post-processing is carried out in this study (Fig. 1f). Because completely cloud-free optical imagery is often difficult to obtain, one final damage map is generated for each ice shelf in each year by selecting and integrating predictions from candidate scenes with the optimal spatial coverage and image quality to achieve complete ROI coverage. This strategy assumes surface damage does not change dramatically over short time intervals and avoids fragmentation of the final product in order to improve dataset consistency for subsequent scientific applications.

For each year, priority is given to predictions derived from a single cloud-free scene that fully covers the ROI. When more than one scene fully covers the ROI in a given year, which occurs only rarely, the corresponding predictions are comparatively evaluated to select the final map. If no cloud-free scene can fully cover the ROI, scenes with a relatively high proportion of valid coverage and more complete coverage of rapidly flowing areas are selected first. Additional scenes that provide complementary coverage of the ROI are then selected for manual merging of the corresponding predictions. Because ice flow can displace surface damage features between acquisition dates, predictions from scenes acquired close in time are prioritized during merging to minimize spatial inconsistencies.

In this study, the final merged prediction is not obtained by first mosaicking the selected scenes and then applying the segmentation model. Instead, predictions from individual selected scenes are merged directly to avoid potential interference from tonal differences at scene boundaries during damage extraction. Manual merging is guided by visual inspection of the source imagery and model predictions, with ice velocity (Rignot et al., 2017) used as an auxiliary reference,

to ensure spatially consistent merged results and preserve local damage structures.

A complete damage map covering the ROI is then obtained for each ice shelf in each year. If complete coverage of the target ice shelf region cannot be achieved, no result is retained for that ice shelf in that year. In a small number of full-ROI maps, a limited number of areas on grounded ice within the ROI but outside the main ice shelf may remain affected by cloud contamination because no suitable cloud-free imagery is available for those areas. As these areas do not affect the usability of the target ice shelf region, the corresponding full-ROI maps are reserved. The final maps are also manually checked against the source imagery and the results from adjacent years. The same scene-selection, merging and quality-control criteria are applied consistently to all ice shelves and years.

2.4.2 Product refinement to ice shelf extent

To facilitate the direct use of the dataset for scientific analysis, the full-ROI maps are further post-processed by manually defining the effective floating ice shelf extent at the corresponding time (Fig. S2). Specifically, the grounding line is fixed based on the MEaSUREs ice shelf extent product (Mouginot et al., 2017), whereas the front is manually adjusted according to the corresponding satellite imagery to exclude detached icebergs, sea ice and other non-target areas that may affect dataset use. This process is assisted by reference products such as IceLines (Baumhoer, 2022; Baumhoer et al., 2023) and MEaSUREs ITS_LIVE Antarctic Ice Sheet Extent Masks (Greene et al., 2024). The same criteria were applied consistently across all ice shelves and years. It should be emphasized that these manually adjusted extents are intended only to improve product usability for ice shelf analysis and should not be interpreted as calving front mapping results. The manual adjustment in this step is limited to defining the effective floating ice-shelf extent and no manual editing of predicted damage pixels or damage boundaries is performed during this process.

Accordingly, two types of products are released to meet different user needs. The first type is constrained to the effective ice shelf extent, whereas the second type covers the full ROI without applying the effective extent constraint. The first type of product is subjected to strict manual inspection and is entirely derived from predictions based on high-quality cloud-free imagery. It can be used directly for scientific analysis of ice shelf surface damage. The second type of product provides more complete spatial coverage. As mentioned in Sect. 2.4.1, a small number of these full-ROI maps may contain very limited areas on grounded ice outside the main ice shelf that are affected by cloud or haze and require additional checking against the source imagery before use.

2.5 Technical validation methods

2.5.1 Evaluation of segmentation model performance

To provide a more comprehensive evaluation of the trained segmentation model, this study uses five metrics: mean intersection over union (mIoU), overall accuracy (OA), precision, recall and F1. mIoU and OA are used to assess overall segmentation performance, whereas precision, recall and F1 are calculated specifically for the damage class to evaluate the model's ability to detect surface damage.

The calculation formulae are as follows:

$$\mathrm{IoU} = \frac{\mathrm{TP}}{\mathrm{TP} + \mathrm{FP} + \mathrm{FN}} \tag{4}$$

$$\mathrm{mIoU} = \frac{1}{2}\sum_{i=1}^{2}\mathrm{IoU}_i \tag{5}$$

$$\mathrm{OA} = \frac{\mathrm{TP} + \mathrm{TN}}{\mathrm{TP} + \mathrm{TN} + \mathrm{FP} + \mathrm{FN}} \tag{6}$$

$$\mathrm{Precision} = \frac{\mathrm{TP}}{\mathrm{TP} + \mathrm{FP}} \tag{7}$$

$$\mathrm{Recall} = \frac{\mathrm{TP}}{\mathrm{TP} + \mathrm{FN}} \tag{8}$$

$$F_1 = 2 \times \frac{\mathrm{Precision} \times \mathrm{Recall}}{\mathrm{Precision} + \mathrm{Recall}} \tag{9}$$

where TP, TN, FP and FN denote true positive, true negative, false positive and false negative, respectively.

The above metrics were calculated for the validation set of the manually annotated dataset. The evaluation was further conducted on a contiguous Landsat 8 scene and a set of Landsat 7 SLC-on image tiles from ice shelves not represented in the training or validation data, to assess the geographic generalizability of the segmentation model and its performance across sensors. Considering the highly consistent spectral band characteristics of the sensors onboard Landsat 8 and Landsat 9, no additional evaluation was conducted for Landsat 9 imagery. The same segmentation metrics are also used to assess the performance of damage mapping on DiffGF-restored Landsat 7 SLC-off imagery, by comparing the segmentation results derived from restored imagery with those derived from the corresponding original imagery.

2.5.2 Multi-temporal consistency assessment

As the availability of usable optical satellite imagery is affected by cloud cover, the acquisition times of the scenes used for dataset generation cannot be kept consistent across different years. In addition, the brightness and local details of optical imagery acquired at different times are affected by factors such as illumination conditions, observation geometry, the physical state of the ice shelf surface and topographic shading. Therefore, differences between damage maps of different years may reflect not only real changes in surface damage but also, in part, objective differences in the

data source. To assess the influence of such source-related differences on the usability of the dataset for temporal analysis, a multi-temporal consistency assessment is carried out.

Considering that damage itself evolves dynamically, including both the formation of new damage and advection with ice flow, independent temporal tracking of all damage features is difficult to achieve. Given that damage density is an important metric in temporal analysis and glaciological modelling, this study performs a density-based multi-temporal consistency assessment of the surface damage maps generated for each ice shelf. We assume that in most years without severe changes, such as disintegration, changes in surface damage on ice shelves are generally gradual, and therefore damage density in temporally adjacent maps should show a certain degree of correlation.

Three metrics are used for multi-temporal consistency assessment, including Spearman's rank correlation coefficient (r_s), Lin's concordance correlation coefficient (CCC, ρ_c) and root mean square error (RMSE). Among them, r_s is used to assess the consistency of the rank of grid cell values in temporally adjacent damage density maps, CCC evaluates their agreement in absolute magnitude and RMSE measures their average numerical deviation. The formulae are as follows:

$$r_s = \frac{\sum_{i=1}^{n} \left(R_i - \overline{R}\right)\left(S_i - \overline{S}\right)}{\sqrt{\sum_{i=1}^{n} \left(R_i - \overline{R}\right)^2 \sum_{i=1}^{n} \left(S_i - \overline{S}\right)^2}} \tag{10}$$

where n is the total number of valid grid cells, R_i and S_i are the ranks of the damage density values at the ith grid cell in two temporally adjacent maps, and $\overline{R}$ and $\overline{S}$ are their respective mean ranks. Tied values are assigned average ranks.

$$\rho_c = \frac{2\sigma_{xy}}{\sigma_x^2 + \sigma_y^2 + \left(\mu_x - \mu_y\right)^2} \tag{11}$$

where μ_x and μ_y are the mean values of damage density for two temporally adjacent density maps, σ_x^2 and σ_y^2 are the variances of the two density maps, and σ_{xy} is the covariance between them.

$$\mathrm{RMSE} = \sqrt{\frac{1}{n}\sum_{i=1}^{n}(x_i - y_i)^2} \tag{12}$$

where n is the total number of valid grid cells and x_i and y_i are the values of the ith grid cell in two temporally adjacent density maps.

Considering the relatively rapid ice flow on ice shelves (especially for Totten, Pine Island and Thwaites), multi-temporal consistency is assessed using damage density maps calculated on a 900 m grid. For each grid cell, damage density is computed as the fraction of damage area within that cell, without resampling the original 30 m damage maps. To account for advection between adjacent time steps, the MEaSUREs InSAR-based ice velocity product at 450 m resolution (Rignot et al., 2017) is used to apply a Lagrangian correction. For each temporally adjacent pair, the earlier damage density map is advected forward to the time of the later map using the ice velocity product, as follows:

$$\boldsymbol{x}_{t+\Delta t} = \boldsymbol{x}_t + \boldsymbol{v}(\boldsymbol{x}_t)\,\Delta t \tag{13}$$

where $\boldsymbol{x}_{t+\Delta t}$ is the corrected grid cell position at the time of the later map, $\boldsymbol{x}_t$ is the original grid cell position in the earlier map, $\boldsymbol{v}(\boldsymbol{x}_t)$ is the ice velocity vector extracted from the ice velocity product at $\boldsymbol{x}_t$, and Δt is the time interval between adjacent maps in years.

The above metrics are then calculated by comparing the Lagrangian-corrected earlier damage density map with the original later damage density map. For comparison, the same metrics are also calculated from the original adjacent damage density maps without Lagrangian correction. Since the temporal coverage and step intervals vary across ice shelves, the median values across all adjacent pairs are used to represent the overall multi-temporal consistency.

3 Results

3.1 Dataset overview

The final dataset contains 170 surface damage maps at a spatial resolution of 30 m, and the temporal coverage for each ice shelf is shown in Fig. 3. Overall, temporal coverage varies among ice shelves, mainly due to the availability of optical imagery in each region. Crosson, Dotson, Pine Island and Thwaites ice shelves in the Amundsen Sea sector have relatively continuous temporal coverage during the study period, with maps available for all years except 2005. The absence of maps for 2005 is due to the lack of Landsat data acquisition during that period. Brunt and Amery ice shelves also have map series beginning earlier, in 2000 and 2003, respectively, although their early temporal coverage is not continuous. In contrast, the available maps for Scar Inlet, Holmes and Totten ice shelves start relatively later. The lack of early maps mainly results from the unstable acquisition quality of some early Landsat 7 imagery (e.g. overexposure), which led to a lack of usable data. However, all ice shelves maintain relatively continuous temporal coverage in the subsequent period. Representative zoomed-in examples of the surface damage maps for each ice shelf are shown in Fig. 7.

3.2 Dataset technical validation

3.2.1 Performance of segmentation model on the validation set

The performance of the trained image segmentation model is evaluated on the validation set of the manually annotated dataset. The quantitative evaluation results on the validation

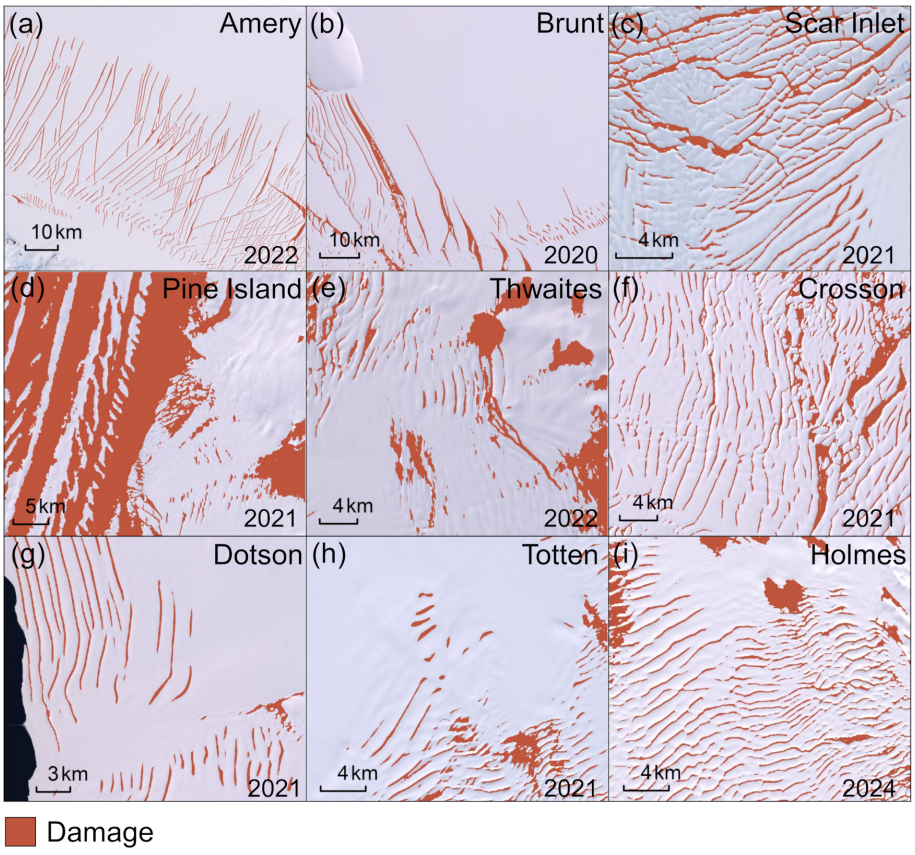


Figure 7. Zoomed-in examples of the surface damage maps for **(a)** Amery, **(b)** Brunt, **(c)** Scar Inlet, **(d)** Pine Island, **(e)** Thwaites, **(f)** Crosson, **(g)** Dotson, **(h)** Totten, and **(i)** Holmes Ice Shelves. The annotated years indicate the sunlit seasons during which the Landsat imagery was acquired.

set are presented in Table 3 and some example results are shown in Fig. 8. As shown in Fig. 8, the model predictions agree well with the manually annotated labels across three diverse validation scenes, with the difference maps dominated by TP and TN (black) pixels and only limited FP (red) and FN (blue) errors, mainly concentrated along damage boundaries. The corresponding prediction entropy maps are further discussed in Sect. 3.2.4. The results indicate that the model achieves good performance in surface damage extraction and is capable of identifying multiple types of surface damage with high accuracy.

3.2.2 Performance of segmentation model on independent test sets

To further evaluate the generalizability of the image segmentation model, two independent test sets were used. First, Totten Ice Shelf, which was not included in either the training or validation set, was selected for an independent ice-shelf test. A Landsat 8 optical image acquired on 23 January 2021 was manually annotated following the same criteria as described in Sect. 2.3.1, and the prediction over the contiguous image extent was evaluated as a whole. As shown in Fig. 9, the prediction is overall consistent with the label, with sparse FN (blue) errors distributed along the edges of damage regions and in damage areas with relatively low image contrast. The evaluation metrics are presented in Table 3. The results indicate that the model maintained good segmentation performance on Totten Ice Shelf, demonstrating its ability to generalize to a geographically independent region.

Second, to evaluate cross-sensor generalization, the trained model was applied to an independent cross-sensor test set comprising Landsat 7 SLC-on imagery. This test set comprised 34 manually annotated 512×512 image tiles from Brunt, Dotson and Thwaites ice shelves (Fig. S1), none of which were included in the training or validation sets. The images were manually annotated following the same criteria, but without the assistance of Sentinel-1 and ICESat-2 data. As shown in Table 3 and Fig. 10, the segmentation model achieved comparable overall performance on the Landsat 7 cross-sensor test set. Together, the results from these two independent test sets provide further evidence for the geographic and cross-sensor generalizability of the segmentation model.

Table 3. Performance of the segmentation model on the validation set and independent test sets. (L8: Landsat 8; L7: Landsat 7; SLC-on: scan-line-corrector-on).

Evaluation set	Sensor	Evaluation extent	mIoU	OA	Precision	Recall	F_1
Validation set	L8	52 tiles	0.845	0.984	0.816	0.841	0.829
Independent ice-shelf test	L8	Contiguous scene	0.822	0.960	0.838	0.792	0.814
Independent cross-sensor test	L7 SLC-on	34 tiles	0.837	0.985	0.799	0.834	0.816

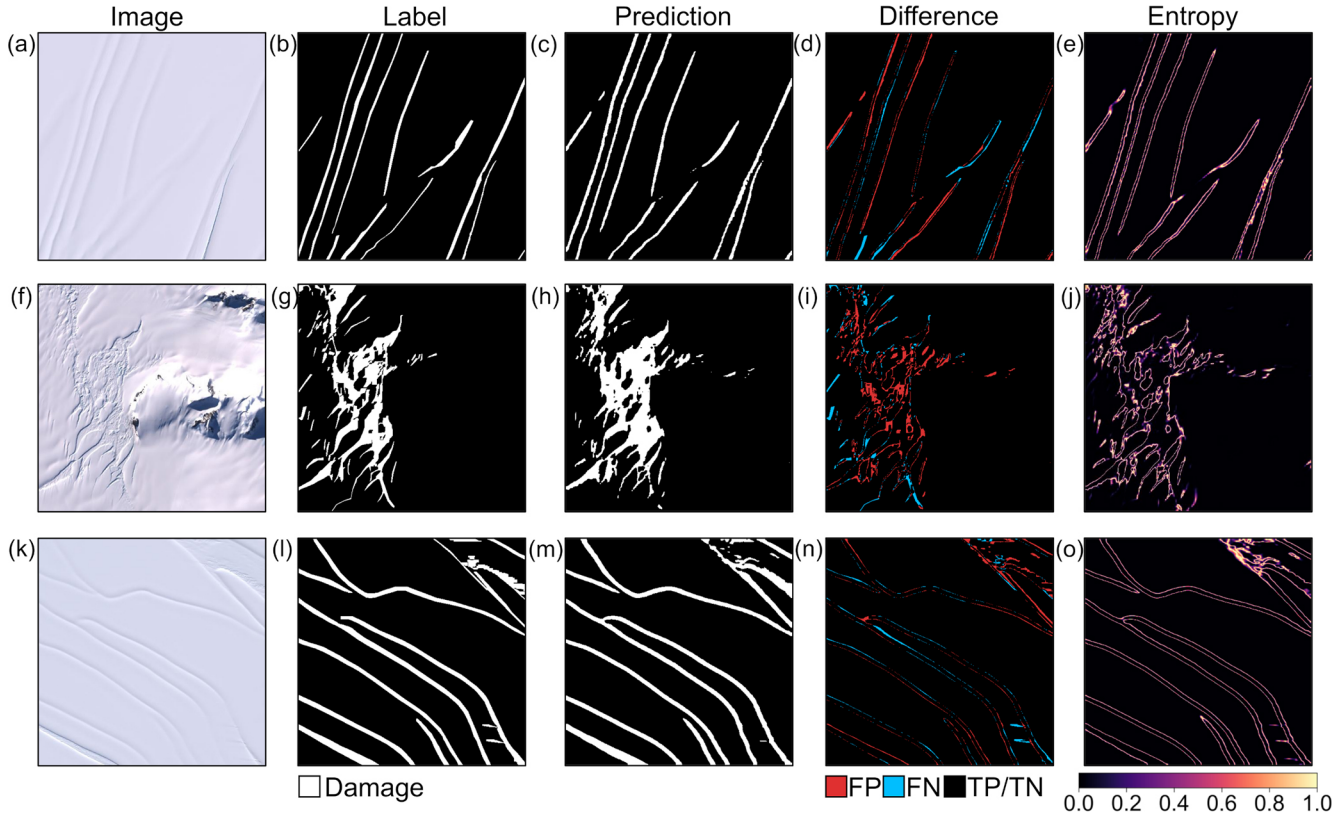


Figure 8. Examples of prediction performance on samples from the validation set. **(a)**, **(f)** and **(k)** show image samples from Amery Ice Shelf, Crosson Ice Shelf and Larsen C Ice Shelf, respectively. **(b)**, **(g)** and **(l)** show the corresponding manually annotated labels. **(c)**, **(h)** and **(m)** show the corresponding model predictions. **(d)**, **(i)** and **(n)** show the pixel-wise difference maps between the corresponding labels and predictions, where TP denotes true positive, FP denotes false positive, FN denotes false negative and TN denotes true negative. **(e)**, **(j)** and **(o)** show the corresponding prediction entropy maps.

3.2.3 Performance of segmentation on restored Landsat 7 SLC-off imagery

The restoration performance of DiffGF on Landsat 7 SLC-off imagery is also evaluated (see Tang et al., 2026b). Scar Inlet Ice Shelf is selected as the primary test case, as it contains multiple types of surface damage and was not included in the training data of either the DiffGF framework or the image segmentation model.

The test imagery is constructed from a Landsat 8 image acquired on 21 December 2021, to which an SLC-off mask extracted from a Landsat 7 SLC-off image acquired on 20 February 2012 at the same location is applied, thereby generating simulated SLC-off imagery with ground-truth reference. DiffGF is then used to restore the simulated SLC-off imagery, and the image segmentation model is applied to the restored imagery for surface damage extraction. The results are shown in Figs. 11, S3 and S4. Image quality metrics between the restored imagery and the ground-truth imagery are reported in Table 4. The restoration metrics are calculated both over the full image and the simulated SLC-off gap areas. The comparison between the segmentation result from the restored imagery and that from the ground-truth imagery is shown in Table 5.

To further assess the applicability of DiffGF across different regions and surface conditions, additional simulated SLC-off tests are conducted using regional test images from

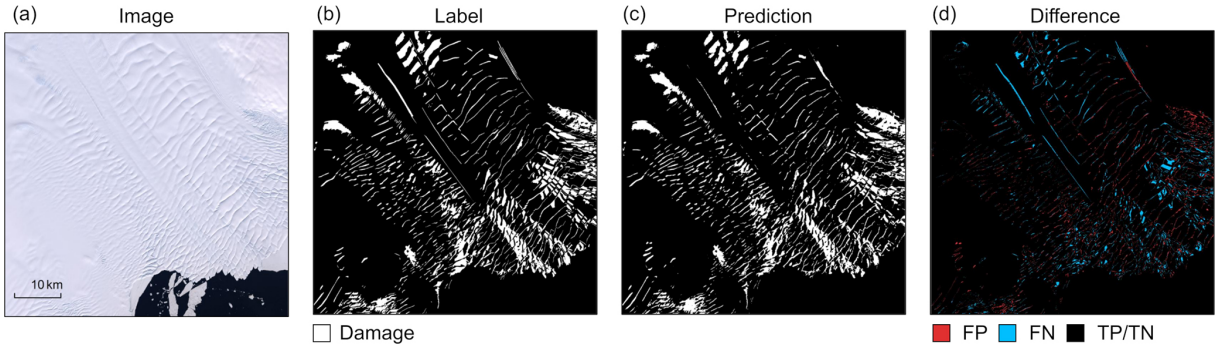


Figure 9. Prediction performance over the full contiguous Landsat 8 test scene on Totten Ice Shelf. **(a)** Landsat 8 image acquired on 23 January 2021. **(b)** Manually annotated label. **(c)** Model prediction. (d) Pixel-wise difference map between label and prediction, where TP denotes true positive, FP denotes false positive, FN denotes false negative and TN denotes true negative.

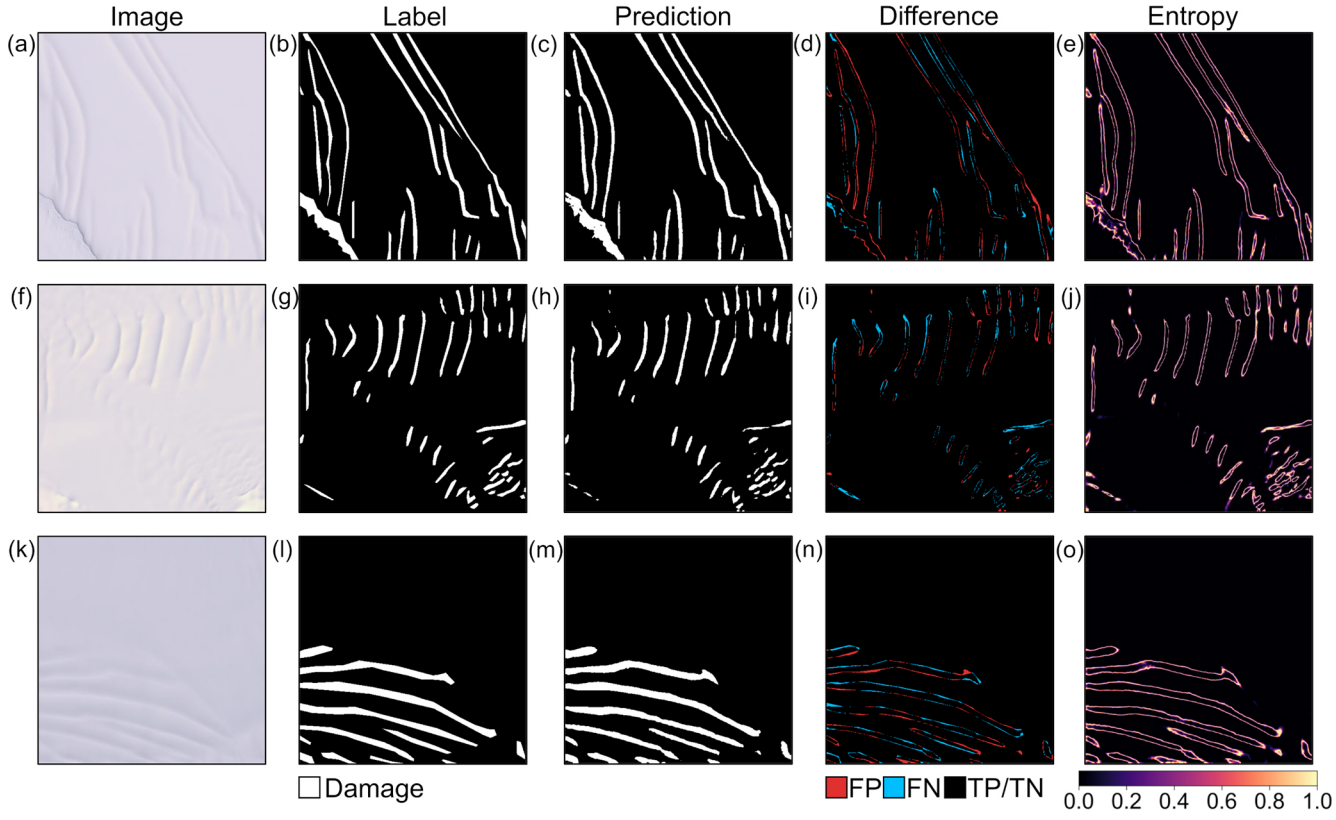


Figure 10. Examples of prediction performance on samples from the Landsat 7 SLC-on cross-sensor test set. **(a)**, **(f)** and **(k)** show image samples from Brunt Ice Shelf, Dotson Ice Shelf and Thwaites Ice Shelf, respectively. **(b)**, **(g)** and **(l)** show the corresponding manually annotated labels. **(c)**, **(h)** and **(m)** show the corresponding model predictions. **(d)**, **(i)** and **(n)** show the pixel-wise difference maps between the corresponding labels and predictions, where TP denotes true positive, FP denotes false positive, FN denotes false negative and TN denotes true negative. **(e)**, **(j)** and **(o)** show the corresponding prediction entropy maps.

Amery, Crosson and Pine Island ice shelves. The corresponding restoration results and surface damage segmentation performance are provided in Figs. S5–S7 and Table S3.

The evaluation on Scar Inlet Ice Shelf indicates that DiffGF achieves good restoration performance in this test case, and that the surface damage segmentation result obtained from the restored imagery (Fig. 11e) is close to that from the ground-truth imagery (Fig. 11d). The additional regional tests also show consistently high segmentation performance on the restored imagery (Table S3). Together, these results provide further support for the use of restored Landsat 7 SLC-off imagery in surface damage mapping.

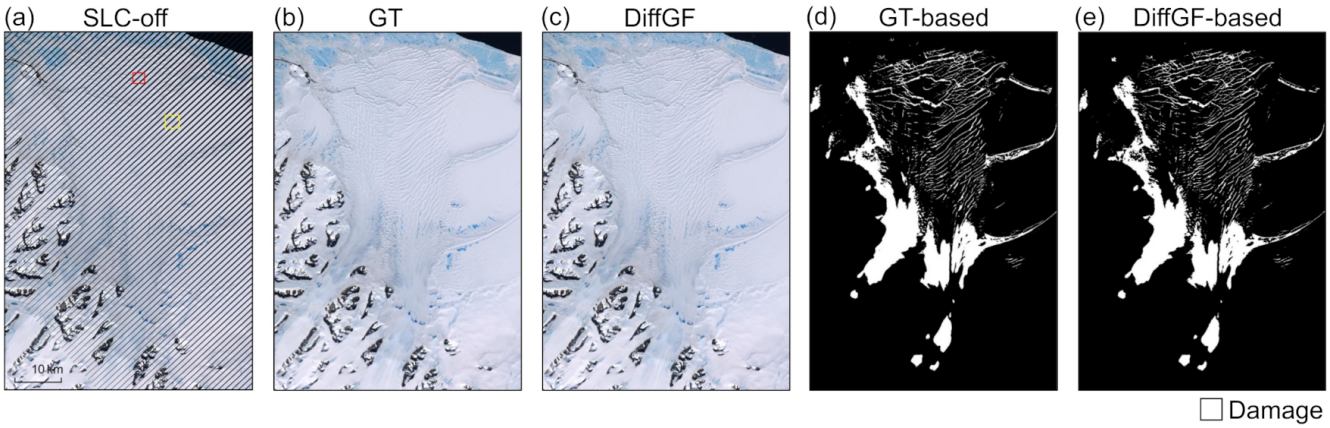


Figure 11. SLC-off restoration performance for Scar Inlet Ice Shelf. **(a)** Simulated SLC-off image with red and yellow boxes indicating zoomed-in regions shown in Figs. S3 and S4. **(b)** Ground truth (GT) image. **(c)** DiffGF-restored image. **(d)** Damage segmentation derived from GT. **(e)** Damage segmentation derived from DiffGF restoration.

Table 4. Image quality metrics of the restored SLC-off test image over the full image and SLC-off gap areas. (LPIPS is calculated only on the full image.)

Extent	PSNR	UIQI	SSIM	CC	RMSE	LPIPS
Full image	35.070	0.994	0.966	0.994	0.018	0.060
SLC-off gaps	27.779	0.962	0.862	0.963	0.041	–

Table 5. Segmentation evaluation of the restored SLC-off test image against the original complete image.

mIoU	OA	Precision	Recall	F_1
0.945	0.989	0.969	0.929	0.948

3.2.4 Uncertainty estimation

This dataset is subject to two main sources of uncertainty: errors introduced during the segmentation process and additional uncertainty associated with damage mapping performed on DiffGF-restored Landsat 7 SLC-off imagery.

For the image segmentation model, uncertainty in damage mapping is quantified using uncertainty scaling factors derived from the model performance evaluation metrics reported in Sect. 3.2.1 and 3.2.2. From Eqs. (7) and (8), it follows that:

$$N_{\text{true}} = \frac{\text{Precision}}{\text{Recall}} N_{\text{pred}}. \tag{14}$$

Therefore, $\frac{\text{Precision}}{\text{Recall}}$ is used as the uncertainty scaling factor λ to derive uncertainty bounds for the mapped damage extent. Based on the evaluation results for the validation set and two independent test sets (Table 3), including both Landsat 8 and Landsat 7 imagery, the minimum value $\lambda_{\min} = 0.958$ and the maximum value $\lambda_{\max} = 1.059$ are used to define the lower and upper uncertainty bounds, respectively.

For results generated from Landsat 7 SLC-off imagery restored by DiffGF, an additional source of uncertainty arises from the restoration process itself. Given the generative nature of the diffusion model, subtle discrepancies between the restored imagery and ground-truth surface conditions can introduce additional uncertainty into the damage mapping results. Based on the accuracy evaluation of the segmentation result from the restored imagery against that from the ground-truth imagery (Table 5), the additional scaling factor associated with DiffGF restoration is $\lambda_{\text{DiffGF}} = 1.044$. To conservatively account for this additional uncertainty, the upper uncertainty bound for results generated from DiffGF-restored imagery is further adjusted to $\lambda_{\max} \times \lambda_{\text{DiffGF}} = 1.105$, whereas the lower uncertainty bound remains unchanged so that the lower side of the uncertainty range is not narrowed.

These bounds should be interpreted as map-level uncertainty estimates for the mapped damage extent rather than spatially explicit pixel-wise error estimates. To complement these map-level estimates with spatial information, prediction entropy maps were generated for representative samples from the validation and cross-sensor test sets (Figs. 8 and 10). Prediction entropy was calculated from the pixel-level class probabilities using the Shannon entropy formula and normalized to the range 0–1. Higher values indicate greater uncertainty in distinguishing damage from background, whereas lower values indicate more confident predictions. The entropy maps show that higher entropy is mainly found along damage boundaries and within regions characterized by complex damage patterns, generally coinciding with the spatial distribution of FP and FN errors in the difference maps.

In addition to the uncertainty sources quantified above, the dataset is also subject to uncertainties that are more difficult to characterize. As described in Sects. 2.4.1 and 2.5.2, the final damage maps are generated through a process that involves manual judgement and can also be affected by im-

Table 6. Multi-temporal consistency metrics for time-series ice shelf surface damage density after applying ice-velocity-based Lagrangian correction.

Ice shelf	Median of r_s	Median of ρ_c	Median of RMSE
Amery (full)	0.756	0.807	0.072
Amery (front)	0.812	0.845	0.040
Brunt	0.816	0.917	0.068
Crosson	0.884	0.913	0.074
Dotson	0.778	0.858	0.039
Holmes	0.872	0.875	0.088
Scar Inlet	0.887	0.950	0.091
Pine Island	0.900	0.929	0.129
Thwaites	0.846	0.862	0.173
Totten	0.893	0.860	0.067

Table 7. Multi-temporal consistency metrics for time-series ice shelf surface damage density without applying Lagrangian correction.

Ice shelf	Median of r_s	Median of ρ_c	Median of RMSE
Amery (full)	0.680	0.723	0.094
Amery (front)	0.639	0.529	0.084
Brunt	0.626	0.812	0.112
Crosson	0.669	0.752	0.140
Dotson	0.810	0.824	0.048
Holmes	0.776	0.834	0.119
Scar Inlet	0.850	0.920	0.109
Pine Island	0.879	0.909	0.155
Thwaites	0.751	0.798	0.214
Totten	0.804	0.702	0.107

agery acquisition conditions across years. To further assess the temporal reliability of the dataset, a multi-temporal consistency assessment is presented in the following section.

3.2.5 Multi-temporal consistency of the dataset

The multi-temporal consistency assessment results of damage density for each ice shelf are shown in Tables 6 and 7. It should be noted that, for Amery Ice Shelf, the assessment is conducted separately for the entire ice shelf (full) and for the frontal region within approximately 240 km of the ice front (front). See Sect. 5 for details.

As shown in Table 6, the multi-temporal consistency of damage density in the surface damage maps is generally good for all ice shelves, with median r_s values ranging from 0.75 to 0.90, median ρ_c values ranging from 0.80 to 0.95, and median RMSE values ranging from 0.04 to 0.17. Among these ice shelves, Pine Island and Thwaites ice shelves exhibit the most pronounced surface damage change over the time span of the dataset, and they also have the highest RMSE values. Compared with the results in Table 7 without Lagrangian correction based on ice velocity, the consistency metrics improve for most ice shelves after correction, as reflected by increases in r_s and ρ_c and decreases in RMSE. The improvement is most pronounced for Amery (front), Brunt and Crosson ice shelves.

For Dotson Ice Shelf, r_s decreases slightly after the Lagrangian correction is applied, indicating a small reduction in the rank-order consistency of damage density values across grid cells between adjacent maps. This is mainly due to the ice flow direction near the boundary between Dotson and Crosson ice shelves (Fig. S14), where ice flows towards Crosson Ice Shelf, causing some pixels to advect beyond the original ice shelf extent after correction and thus affecting this rank-based correlation metric. In addition, ice flow on Dotson Ice Shelf is relatively slow, and the damage density maps already exhibit high temporal consistency without correction. Therefore, after correction, the exclusion of pixels near the boundary leads to a slight decrease in r_s. Apart from this special case, no similar phenomenon is observed for the other ice shelves.

Overall, the dataset shows good multi-temporal consistency across temporally adjacent pairs. The improvement in consistency metrics after applying the Lagrangian correction further indicates that the temporal variations captured in the dataset are physically consistent with ice advection, providing additional evidence for the reliability of the mapped changes in surface damage. This multi-temporal consistency assessment therefore supports the use of the dataset for subsequent temporal analysis, although variations in image acquisition conditions and surface conditions may still affect the detectability of individual damage features.

3.2.6 Comparison with existing approaches

The dataset is also compared with other existing approaches. Among the publicly available surface damage detection algorithms, only NeRD (Izeboud and Lhermitte, 2023; Izeboud et al., 2025) is applicable to the data source used in this study, and is therefore selected for comparison by processing the same optical imagery. In addition, the 100 m resolution surface damage map of Antarctic ice shelves derived from Sentinel-1 SAR images for June 2021 by Surawy-Stepney et al. (2023b) using a deep-learning method is also selected for comparison.

Landsat 8 optical images of Thwaites (21 November 2020) and Crosson (12 December 2020) ice shelves are selected for comparison, as they contain multiple types of surface damage features and provide a comprehensive illustration of the differences among methods and products (Fig. 12). None of the selected imagery is used in the training of the image segmentation model.

For the NeRD method, the official implementation provided by Izeboud and Lhermitte (2023) is used. A window size of 5 pixels is selected for this comparison, yielding an

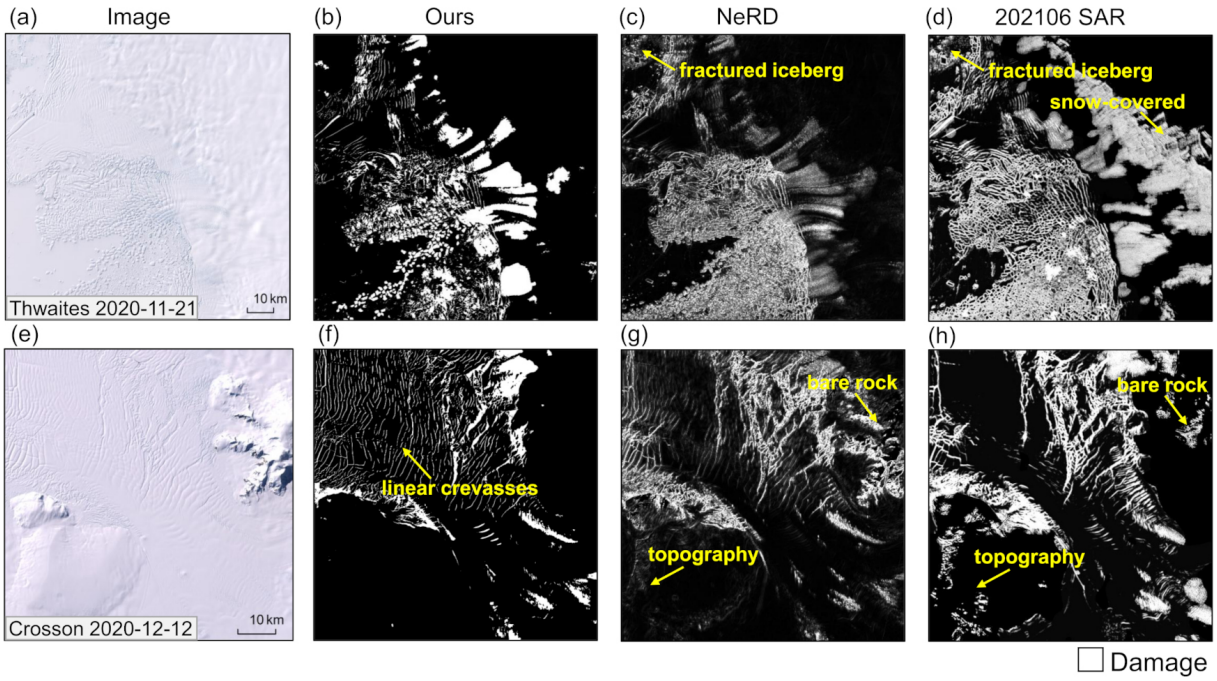


Figure 12. Comparison of the generated dataset with existing approaches. **(a)** and **(e)** show optical images of Thwaites Ice Shelf and Crosson Ice Shelf, respectively. **(b)** and **(f)** show the results of this dataset. **(c)** and **(g)** show the results generated by NeRD (Izeboud and Lhermitte, 2023). **(d)** and **(h)** show the released SAR-based map for June 2021 (Surawy-Stepney et al., 2023b). The results of this dataset are displayed as binary values of 0 and 1, whereas the NeRD and SAR-based results for June 2021 are displayed in the range [0, 1] with standard deviation stretch applied to enhance visual clarity.

output spatial resolution of 150 m. Given the differing spatial resolutions across products, only qualitative comparison is performed. Our results are generally consistent with those of NeRD, showing good agreement in both the extraction of linear damage and heavily fractured areas. Furthermore, because the training dataset includes samples of features that resemble surface damage, such as edges associated with bare rock and local topography, our model successfully distinguishes true damage from structurally similar non-damage features (Fig. 12). Our model also correctly excludes small icebergs that are falsely identified as surface damage in the other two results. In addition, the inference speed of our deep-learning model is substantially faster than that of the image-processing-based NeRD method. For the Thwaites Ice Shelf image shown in Fig. 12a (3584×3584 pixels, covering approximately 107 km × 107 km), our approach requires 22 s for inference, whereas NeRD requires approximately 40 min on the same device, representing a speedup of over 100×.

Compared with the SAR-derived surface damage map for June 2021, our results show better agreement with the SAR-based product over Thwaites Ice Shelf than over Crosson. In areas landward of the grounding line, snow-covered damage that is difficult to detect in optical imagery can be identified by SAR data owing to its penetration capability (Fig. 12d). On Crosson Ice Shelf, our method is able to identify dense linear crevasses that are absent from the SAR-based product (Fig. 12f), primarily because these features are more clearly characterized in optical imagery. Similar to the NeRD results, the SAR-based product also misidentifies some edge features associated with bare rock and local topography as damage (Fig. 12h). Such misclassification may be related to the training strategy of Surawy-Stepney et al. (2023b), where the model was initially trained on manually annotated calving fronts and may therefore be more sensitive to linear features. The limited spectral information available from single-band SAR data may further increase the difficulty in distinguishing surface damage from edge features with similar backscatter responses. Nevertheless, such misclassification can be mitigated through post-processing using a bare rock dataset and an ice shelf extent mask.

Overall, our results show high consistency with those of NeRD (Izeboud and Lhermitte, 2023) when using the same optical data source, while providing higher spatial resolution and substantially improved computational efficiency. Compared with the SAR-based results of Surawy-Stepney et al. (2023b), our results show good agreement for damage features visible in both data sources, and also provide higher spatial resolution. Compared with existing approaches, the deep-learning-based method used in this study achieves good extraction performance with high computational efficiency, making it well suited to large-area, long-term dataset production. In addition, the use of Landsat RGB imagery in this

study enables richer spectral characterization of surface damage and makes it possible to extend the time-series mapping back to 1999.

3.3 Time-series characteristics of surface damage

To characterize the temporal variation in surface damage development for each ice shelf over the study period, surface damage area and surface damage fraction are calculated for each map. The formula for calculating damage fraction is as follows:

$$\text{damage fraction} = \frac{\text{damage area}}{\text{ice shelf area}} \tag{15}$$

where ice shelf area is the area of the manually delineated ice shelf extent for the corresponding period. Readers may also calculate the corresponding damage fraction using their own customized ice shelf extent.

The temporal variations of surface damage fraction and area are shown in Fig. 13, with shaded regions indicating the uncertainty bounds estimated in Sect. 3.2.4. For the damage fraction, uncertainty in the ice shelf area was not included in these shaded bounds. Overall, the nine ice shelves can be broadly grouped into two categories based on the magnitude of temporal change in surface damage. The first category includes Pine Island, Thwaites and Scar Inlet ice shelves, which show relatively large changes in surface damage fraction during the study period (Figs. 13a and 14–16). The remaining ice shelves fall into the second category, where surface damage shows less pronounced temporal change during this period (Figs. 17, S10 and S12–S16).

Among the ice shelves with more pronounced surface damage change, Pine Island (Fig. 14) and Scar Inlet (Fig. 16) show clear development of new damage, with the ice shelf surface becoming progressively more damaged along the main ice flow direction and in shear margin areas. These patterns are consistent with the documented accelerated flow and instability of these ice shelves (Lhermitte et al., 2020; Joughin et al., 2021; Qiao et al., 2020; Ochwat et al., 2024). Thwaites also shows pronounced changes (Fig. 15). Thwaites West Ice Tongue (TWIT) undergoes intense fragmentation and disintegration during the study period, whereas surface damage continues to increase on Thwaites East Ice Shelf (TEIS). These changes are in line with the reported structural weakening of Thwaites Ice Shelf (Benn et al., 2022; Wang et al., 2025). For further analysis of Thwaites, readers are advised to use the full-ROI damage maps, which have a larger effective data domain, for customized analysis.

Among the ice shelves with less pronounced surface damage change, the results still capture the evolution of surface damage and changes associated with calving. These characteristics are reflected in the mapped spatial distribution of damage and the temporal variations (e.g., Amery Ice Shelf, Figs. S10 and S12, and Holmes Ice Shelf, Fig. S15). Brunt Ice Shelf has a larger overall area than other ice shelves in this dataset, so even though calving events occur during the study period, the resulting changes in damage fraction and area are relatively modest. Nevertheless, the results capture increased damage within the shear margin areas and clearly reflect the morphology of rifts prior to calving (Fig. 17).

These example analyses demonstrate that this dataset can characterize the temporal evolution of surface damage on ice shelves and the details of specific change events, thereby contributing to the understanding of ice shelf dynamics.

4 Usage notes

In the released dataset, each ice shelf is stored in a separate folder, and within each folder a subfolder is provided for each available year. An example path is:

[Ice_Shelf_Name]/[YYYY]

Each yearly subfolder stores the surface damage maps for the corresponding ice shelf and year. According to the two product types defined in Sect. 2.4.2, each yearly subfolder contains two types of product files.

The first type of product file is named:

[Sensor]_[Ice_Shelf_Name]_[YYYY](_slc_off_DiffGF)_damage_map.tif

The second type of product file is named:

[Sensor]_[Ice_Shelf_Name]_[YYYY](_slc_off_DiffGF)_damage.tif

In the [Sensor] field, "LE07", "LC08" and "LC09" indicate that the result is derived from Landsat 7, Landsat 8 and Landsat 9 imagery, respectively. If the filename contains more than one [Sensor] value, this indicates that the result was derived from imagery acquired by more than one satellite. If the filename contains "_slc_off_DiffGF", this indicates that the corresponding data source is DiffGF-restored Landsat 7 SLC-off imagery.

All GeoTIFF files are internally compressed using LZW compression and stored as single-band unsigned 8-bit integer (UInt8) raster files at 30 m spatial resolution in the WGS 84/Antarctic Polar Stereographic projection (EPSG:3031). The first type includes only the results within the effective ice shelf extent, where 0 indicates background, 1 indicates damage, and areas outside the effective extent are set to No-Data (255). The second type includes results for the full ROI, where 0 indicates background and 255 indicates damage, without applying the effective extent constraint.

As described in Sect. 2.4.2, the second type of product requires additional manual checking against the corresponding source imagery before use.

In addition, the root folder includes a metadata.ods file recording the acquisition dates of the imagery used to generate the results. The ROIs used for imagery download are provided as GeoPackage files.

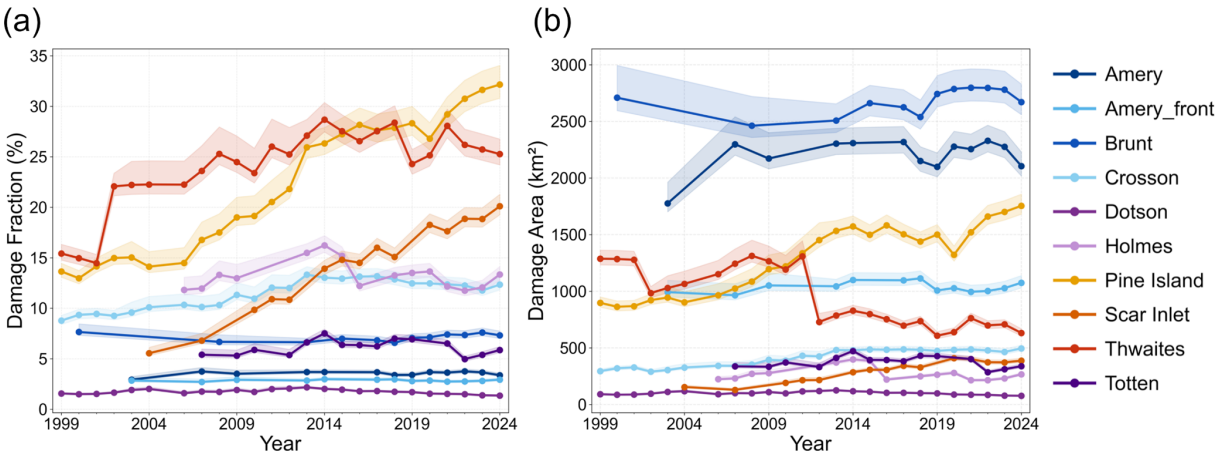


Figure 13. Temporal variations in damage fraction **(a)** and damage area **(b)** for the ice shelves in the dataset during 1999–2024. Colour-vision-deficiency-friendly versions of this figure are provided in Figs. S8 and S9.

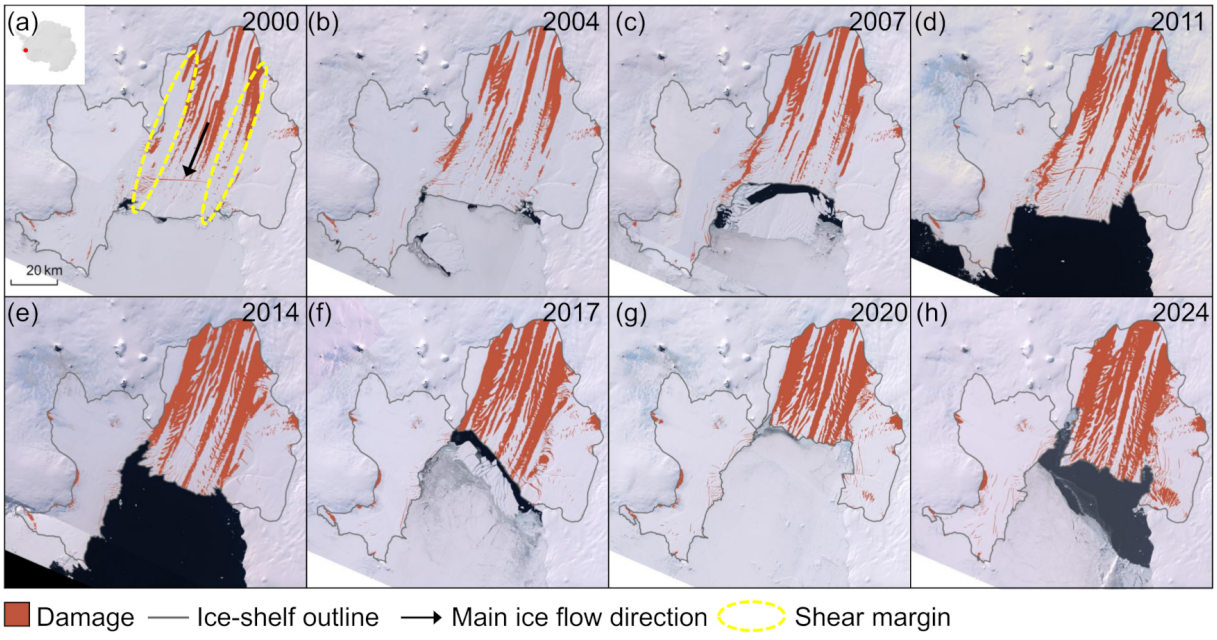


Figure 14. Representative surface damage maps of Pine Island Ice Shelf for **(a)** 2000, **(b)** 2004, **(c)** 2007, **(d)** 2011, **(e)** 2014, **(f)** 2017, **(g)** 2020 and **(h)** 2024. The location of Pine Island Ice Shelf in Antarctica is shown in **(a)**.

5 Discussion

This dataset provides a high-resolution long-term record of surface damage mapping for ice shelves since 1999 and offers new insights into Antarctic ice shelf stability. Compared with products at the 1 km scale that identify whether damage signals are present within each pixel (Izeboud et al., 2025), this dataset has a higher spatial resolution of 30 m, enabling better preservation of the morphological characteristics of damage features. At 1 km resolution, surface damage is significantly aggregated and finer damage features remain undetected, which may obscure the early-stage damage development. Our dataset therefore supports more detailed temporal analysis of damage evolution at finer spatial scales. Previous studies have shown that incorporating damage evolution into numerical ice flow models can substantially improve projections of ice mass loss, but large uncertainties remain in the associated parameters (Ranganathan et al., 2025). The high-resolution time-series surface damage maps produced in our study document the spatial distribution and temporal evolution of observable surface damage and may help interpret patterns of ice weakening inferred from ice-flow inversions and evaluate simulated damage evolution.

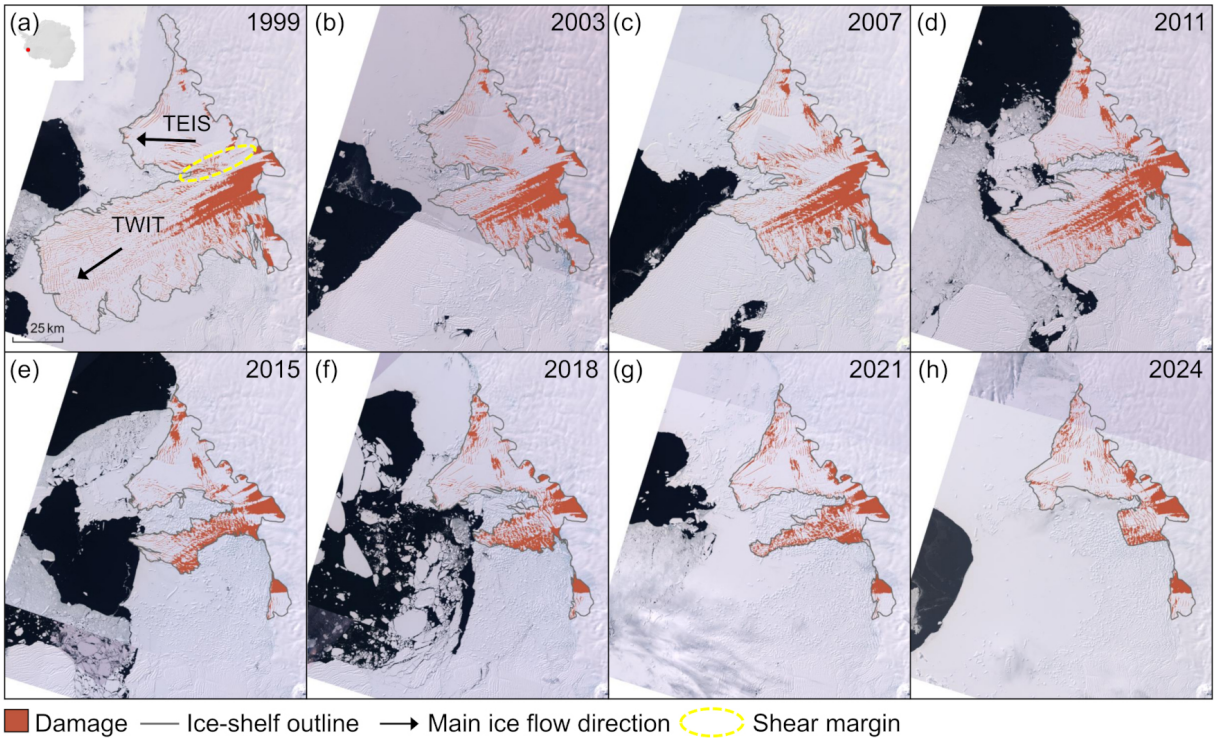


Figure 15. Representative surface damage maps of Thwaites Ice Shelf for **(a)** 1999, **(b)** 2003, **(c)** 2007, **(d)** 2011, **(e)** 2015, **(f)** 2018, **(g)** 2021 and **(h)** 2024. The location of Thwaites Ice Shelf in Antarctica is shown in **(a)**.

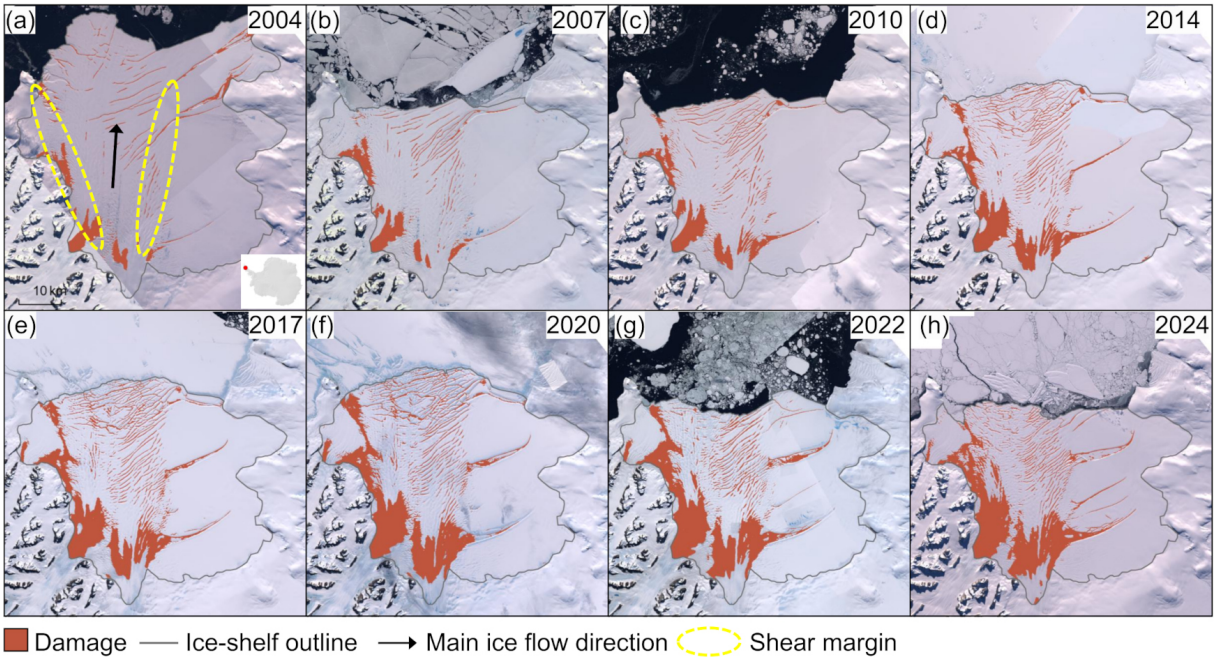


Figure 16. Representative surface damage maps of Scar Inlet Ice Shelf for **(a)** 2004, **(b)** 2007, **(c)** 2010, **(d)** 2014, **(e)** 2017, **(f)** 2020, **(g)** 2022 and **(h)** 2024. The location of Scar Inlet Ice Shelf in Antarctica is shown in **(a)**.

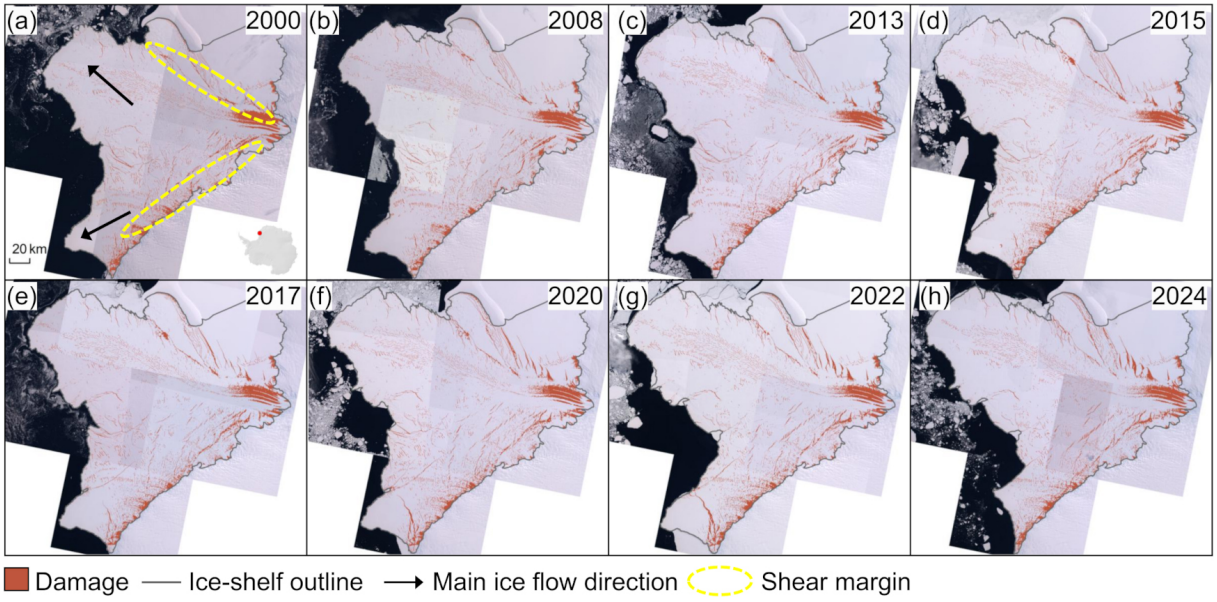


Figure 17. Representative surface damage maps of Brunt Ice Shelf for **(a)** 2000, **(b)** 2008, **(c)** 2013, **(d)** 2015, **(e)** 2017, **(f)** 2020, **(g)** 2022 and **(h)** 2024. The location of Brunt Ice Shelf in Antarctica is shown in **(a)**.

To generate observations over a long time span with high temporal continuity, Landsat optical imagery is used as the data source for the period 1999–2024, considering public availability, spatial resolution and temporal consistency. The availability of optical imagery is limited by cloud cover, and usable imagery can only be acquired during the sunlit season in Antarctica. As this study focuses on long-term damage evolution, this temporal sampling is considered appropriate for the intended application of the dataset. However, the identification of individual damage features in the annual products may still be affected by seasonal snow bridging over crevasses and variations in imaging conditions such as illumination angle. The generally good multi-temporal consistency of the dataset suggests that these variations do not dominate the mapped temporal patterns. Sensitivity to such variations may, however, be greater in grounded ice areas, where surface damage is generally shallower. These areas are not included in the first type of product, and results from the second type of product (full-ROI) in such regions should therefore be interpreted with caution. Another aspect of uncertainty concerns the delineation of damage boundaries. Inspection of the difference maps (Figs. 8–10) shows that most false-positive and false-negative pixels occur along damage boundaries, which is also reflected by the higher prediction uncertainty along these boundaries in the entropy maps.

Although the 30 m resolution of Landsat imagery is relatively high among openly available multi-decadal Earth observation datasets, it remains challenging at this scale to distinguish densely distributed damage features individually. This phenomenon is especially pronounced in regions such as the Pine Island ice tongue, where continuous and densely clustered surface damage often appears in Landsat imagery as contiguous rough-textured areas (Fig. 14). As shown in Fig. S17, airborne high-resolution images (Operation IceBridge CAMBOT L1B Geolocated Images, 10 cm resolution; Studinger and Harbeck, 2019), together with triangulated irregular network (TIN) examples derived from airborne altimetry data (Operation IceBridge ATM L1B Elevation and Return Strength; Studinger, 2013), indicate that such contiguous areas in Landsat imagery correspond to actual linear damage features and surface depressions. On this basis, for densely clustered damage features that cannot be reliably separated from each other at 30 m resolution, this study adopts a connected-region annotation strategy (Fig. 5h). In addition, different types of surface damage are not distinguished in this dataset. The single-class approach was adopted to prioritize the reliability and temporal consistency of damage mapping, as further classification could not be consistently validated using the available observations. Surface expressions associated with basal crevasses may also be included in the maps, as basal crevasses can induce surface deformation and associated surface crevassing through hydrostatic adjustment and the resulting bending stresses (McGrath et al., 2012). Further differentiation of damage types would provide additional information for investigating different mechanisms of damage formation, but requires evidence from other data sources such as basal melt rates, ice thickness, and ocean temperature, which remains an active area for future research. For numerical modelling applications, the distinction between observable surface damage and the damage variables used in numerical models should also be noted.

Among the ice shelves included in the dataset, Amery Ice Shelf is strongly affected by surface meltwater, especially in the area near the southern grounding line, where both seasonal and interannual variations in surface meltwater and stream networks (Surawy-Stepney et al., 2023b; Spergel et al., 2021) can interfere with damage extraction (Figs. S10 and S11). This also contributes to the apparent increase in damage area for Amery Ice Shelf during 2003–2007 (Fig. 13b). A subregional product covering the frontal ~ 240 km of the ice shelf (Amery_front) is therefore also released, and it shows a more stable representation of damage evolution near the calving front (Fig. S12 and Tables 6 and 7). No similar influence is evident for the other ice shelves included in the dataset.

6 Code and data availability

The code used in this study, including the Google Earth Engine scripts for Landsat image acquisition, the surface damage mapping inference code, and the scripts for generating the temporal variation analysis shown in Fig. 13, is available at https://github.com/tly-code/surface-damage-seg and https://doi.org/10.5281/zenodo.24334784 (Tang, 2026a). The code for the DiffGF framework is available at https://github.com/tly-code/DiffGF and https://doi.org/10.5281/zenodo.24334780 (Tang, 2026b). The surface damage dataset generated in this study is available from Zenodo at https://doi.org/10.5281/zenodo.20425951 (v2, Tang et al., 2026a).

7 Conclusions

This study produces a long-term surface damage dataset for nine representative Antarctic ice shelves based on Landsat optical imagery for the period 1999–2024. The dataset contains 170 maps at a spatial resolution of 30 m. During dataset generation, a deep-learning image segmentation model is used for automatic extraction of surface damage. For Landsat 7 SLC-off imagery used during 2003–2013, pre-processing is carried out using a diffusion-model-based non-reference restoration framework.

Validation results from independent test sets indicate that the image segmentation model used in this study has good performance in extracting surface damage. Validation of Landsat 7 SLC-off imagery restored by DiffGF shows that it can serve as a reliable data source for mapping in this dataset. Qualitative comparison with the NeRD method (Izeboud and Lhermitte, 2023) and a SAR-based product (Surawy-Stepney et al., 2023b) shows our dataset is generally consistent with existing approaches, while providing higher spatial resolution and temporal continuity compared to currently available long-term products. The processing workflow developed in this study can be extended to additional regions, supporting Antarctic-wide, long-term mapping of surface damage on ice shelves.

The dataset shows that, among the nine ice shelves studied, Pine Island, Thwaites and Scar Inlet ice shelves experience the most pronounced changes in surface damage during the study period. Surface damage on Pine Island and Scar Inlet ice shelves continues to increase, while Thwaites Ice Shelf shows both significant disintegration processes and increasing surface damage over the same period. Brunt Ice Shelf also shows increased damage in the shear margin areas, whereas the remaining ice shelves remain relatively stable during the study period. The dataset and results presented in this study offer new insights into the temporal evolution of surface damage on Antarctic ice shelves and can help improve current understanding of Antarctic Ice Sheet instability.

Supplement. The supplement related to this article is available online at https://doi.org/10.5194/essd-18-8591-2026-supplement.

Author contributions. Conceptualization: LT and JLB. Data curation: LT. Formal analysis: LT, JLB and TL. Methodology: LT and JLB. Software: LT. Supervision: JLB and GQ. Validation: LT, JLB, TL and GQ. Visualization: LT and TL. Writing (original draft): LT. Writing (review and editing): LT, JLB, TL and GQ.

Competing interests. The contact author has declared that none of the authors has any competing interests.

Disclaimer. Publisher's note: Copernicus Publications remains neutral with regard to jurisdictional claims made in the text, published maps, institutional affiliations, or any other geographical representation in this paper. The authors bear the ultimate responsibility for providing appropriate place names. Views expressed in the text are those of the authors and do not necessarily reflect the views of the publisher.

Acknowledgements. This work was carried out using the computational facilities of the Advanced Computing Research Centre, University of Bristol (http://www.bristol.ac.uk/acrc/, last access: 18 November 2026).

We thank the USGS for providing the Landsat 7/8/9 imagery.

During the preparation of this manuscript, ChatGPT was used in order to enhance the readability. After using this tool, the authors reviewed and edited the content as needed and take full responsibility for the content of the publication.

Financial support. This work is supported by the National Natural Science Foundation of China (grant nos. 42276249 and 42394131), the Science and Technology Commission of Shanghai Municipality (grant no. 23230712200), the Top-notch

Project under the 2024 Shanghai Oriental Talents Program (grant no. BJJY2024049), and the Fundamental Research Funds for the Central Universities (grant no. 22120230311).

Tian Li is funded by the Leverhulme Early Career Fellowship (grant no. ECF-2024-157).

Review statement. This paper was edited by Yufang Ye and reviewed by Sepideh Jalayer, Ted Scambos, and two anonymous referees.

References

Bassis, J., Crawford, A., Kachuck, S., Benn, D., Walker, C., Millstein, J., Duddu, R., Åström, J., Fricker, H., and Luckman, A.: Stability of Ice Shelves and Ice Cliffs in a Changing Climate, Annu. Rev. Earth Planet. Sci., 52, 221–247, https://doi.org/10.1146/annurev-earth-040522-122817, 2024.

Baumhoer, C.: IceLines – Sentinel-1 – Antarctica, German Aerospace Center (DLR) [data set], https://doi.org/10.15489/BTC4QU75GR92, 2022.

Baumhoer, C. A., Dietz, A. J., Heidler, K., and Kuenzer, C.: IceLines – A new data set of Antarctic ice shelf front positions, Sci. Data, 10, 138, https://doi.org/10.1038/s41597-023-02045-x, 2023.

Benn, D., Luckman, A., Åström, J., Crawford, A., Cornford, S., Bevan, S., Zwinger, T., Gladstone, R., Alley, K., Pettit, E., and Bassis, J.: Rapid fragmentation of Thwaites Eastern Ice Shelf, The Cryosphere, 16, 2545–2564, https://doi.org/10.5194/tc-16-2545-2022, 2022.

Borstad, C., Khazendar, A., Larour, E., Morlighem, M., Rignot, E., Schodlok, M., and Seroussi, H.: A damage mechanics assessment of the Larsen B ice shelf prior to collapse: Toward a physically-based calving law, Geophys. Res. Lett., 39, L18502, https://doi.org/10.1029/2012gl053317, 2012.

Chen, L.-C., Zhu, Y., Papandreou, G., Schroff, F., and Adam, H.: Encoder-decoder with atrous separable convolution for semantic image segmentation, European Conference on Computer Vision (ECCV) 2018, 833–851, https://doi.org/10.1007/978-3-030-01234-2_49, 2018.

Colgan, W., Rajaram, H., Abdalati, W., McCutchan, C., Mottram, R., Moussavi, M., and Grigsby, S.: Glacier crevasses: Observations, models, and mass balance implications, Rev. Geophys., 54, 119–161, https://doi.org/10.1002/2015rg000504, 2016.

Davison, B., Hogg, A., Gourmelen, N., Jakob, L., Wuite, J., Nagler, T., Greene, C., Andreasen, J., and Engdahl, M.: Annual mass budget of Antarctic ice shelves from 1997 to 2021, Sci. Adv., 9, eadi0186, https://doi.org/10.1126/sciadv.adi0186, 2023.

EROS – Earth Resources Observation and Science – Center: Landsat 7 Enhanced Thematic Mapper Plus Level-1, Collection 2, US Geological Survey [data set], https://doi.org/10.5066/P9TU80IG, 2020a.

EROS – Earth Resources Observation and Science – Center: Landsat 8–9 Operational Land Imager/Thermal Infrared Sensor Level-1, Collection 2, US Geological Survey [data set], https://doi.org/10.5066/P975CC9B, 2020b.

Francis, D., Mattingly, K. S., Lhermitte, S., Temimi, M., and Heil, P.: Atmospheric extremes caused high oceanward sea surface slope triggering the biggest calving event in more than 50 years at the Amery Ice Shelf, The Cryosphere, 15, 2147–2165, https://doi.org/10.5194/tc-15-2147-2021, 2021.

Fretwell, P., Pritchard, H., Vaughan, D., Bamber, J., Barrand, N., Bell, R., Bianchi, C., Bingham, R., Blankenship, D., Casassa, G., Catania, G., Callens, D., Conway, H., Cook, A., Corr, H., Damaske, D., Damm, V., Ferraccioli, F., Forsberg, R., Fujita, S., Gim, Y., Gogineni, P., Griggs, J., Hindmarsh, R., Holmlund, P., Holt, J., Jacobel, R., Jenkins, A., Jokat, W., Jordan, T., King, E., Kohler, J., Krabill, W., Riger-Kusk, M., Langley, K., Leitchenkov, G., Leuschen, C., Luyendyk, B., Matsuoka, K., Mouginot, J., Nitsche, F., Nogi, Y., Nost, O., Popov, S., Rignot, E., Rippin, D., Rivera, A., Roberts, J., Ross, N., Siegert, M., Smith, A., Steinhage, D., Studinger, M., Sun, B., Tinto, B., Welch, B., Wilson, D., Young, D., Xiangbin, C., and Zirizzotti, A.: Bedmap2: improved ice bed, surface and thickness datasets for Antarctica, The Cryosphere, 7, 375–393, https://doi.org/10.5194/tc-7-375-2013, 2013.

Fretwell, P., Fremand, A., Bodart, J., Pritchard, H., Vaughan, D., Bamber, J., Barrand, N., Bell, R. E., Bianchi, C., Bingham, R., Blankenship, D., Casassa, G., Catania, G., Callens, D., Conway, H., Cook, A., Corr, H., Damaske, D., Damn, V., Ferraccioli, F., Forsberg, R., Fujita, S., Gim, Y., Gogineni, P., Griggs, J., Hindmarsh, R., Holmlund, P., Holt, J. W., Jacobel, R., Jenkins, A., Jokat, W., Jordan, T., King, E., Kohler, J., Krabill, W., Riger-Kusk, M., Langley, K., Leitchenkov, G., Leuschen, C., Luyendyk, B., Matsuoka, K., Mouginot, J., Nitsche, F., Nogi, Y., Nost, O., Popov, S., Rignot, E., Rippin, D., Rivera, A., Roberts, J. L., Ross, N., Siegert, M., Smith, A., Steinhage, D., Studinger, M., Sun, B., Tinto, K., Welch, B., Wilson, D. S., Young, D., Xiangbin, C., and Zirizzotti, A.: BEDMAP2 – Ice thickness, bed and surface elevation for Antarctica – standardised data points, NERC EDS UK Polar Data Centre [data set], https://doi.org/10.5285/2FD95199-365E-4DA1-AE26-3B6D48B3E6AC, 2022.

Fricker, H. A., Galton-Fenzi, B. K., Walker, C. C., Freer, B. I. D., Padman, L., and DeConto, R.: Antarctica in 2025: Drivers of deep uncertainty in projected ice loss, Science, 387, 601–609, https://doi.org/10.1126/science.adt9619, 2025.

Glasser, N. and Scambos, T.: A structural glaciological analysis of the 2002 Larsen B ice-shelf collapse, J. Glaciol., 54, 3–16, https://doi.org/10.3189/002214308784409017, 2008.

Greene, C. A., Gardner, A. S., Schlegel, N.-J., and Fraser, A. D.: Antarctic calving loss rivals ice-shelf thinning, Nature, 609, 948–953, https://doi.org/10.1038/s41586-022-05037-w, 2022.

Greene, C. A., Gardner, A. S., Schlegel, N., and Fraser, A. D.: MEaSUREs ITS_LIVE Antarctic Annual 240 m Ice Sheet Extent Masks, 1997–2021, Version 1, NASA National Snow and Ice Data Center Distributed Active Archive Center [data set], https://doi.org/10.5067/9ZFX84T5GI6D, 2024.

Herzfeld, U., Trantow, T., Lawson, M., Hans, J., and Medley, G.: Surface heights and crevasse morphologies of surging and fast-moving glaciers from ICESat-2 laser altimeter data – Application of the density-dimension algorithm (DDA-ice) and evaluation using airborne altimeter and Planet SkySat data, Sci. Remote Sens., 3, 100013, https://doi.org/10.1016/j.srs.2020.100013, 2021.

Horé, A. and Ziou, D.: Image Quality Metrics: PSNR vs. SSIM, 2010 20th International Conference on Pattern Recognition, 2366–2369, https://doi.org/10.1109/ICPR.2010.579, 2010.

Howat, I., Porter, C., Smith, B., Noh, M., and Morin, P.: The Reference Elevation Model of Antarctica, The Cryosphere, 13, 665–674, https://doi.org/10.5194/tc-13-665-2019, 2019.

Howat, I., Porter, C., Noh, M.-J., Husby, E., Khuvis, S., Danish, E., Tomko, K., Gardiner, J., Negrete, A., Yadav, B., Klassen, J., Kelleher, C., Cloutier, M., Bakker, J., Enos, J., Arnold, G., Bauer, G., and Morin, P.: The Reference Elevation Model of Antarctica – Mosaics, Version 2, Harvard Dataverse [data set], https://doi.org/10.7910/DVN/EBW8UC, 2022.

Huang, Z., Wang, S., Alley, R., Li, A., and Parizek, B.: A Novel Deep Learning-Based Approach for Rift and Iceberg Recognition From ICESat-2 Data, IEEE T. Geosci. Remote, 62, 4300917, https://doi.org/10.1109/tgrs.2024.3382573, 2024.

Huang, Z., Wang, S., Alley, R. B., and Parizek, B. R.: A robust multitask deep learning algorithm for Antarctic ice shelf fracture detection from multisource satellite imagery, Remote Sens. Environ., 330, 114964, https://doi.org/10.1016/j.rse.2025.114964, 2025.

Hulbe, C., LeDoux, C., and Cruikshank, K.: Propagation of long fractures in the Ronne Ice Shelf, Antarctica, investigated using a numerical model of fracture propagation, J. Glaciol., 56, 459–472, https://doi.org/10.3189/002214310792447743, 2010.

Izeboud, M. and Lhermitte, S.: Damage detection on Antarctic ice shelves using the normalised radon transform, Remote Sens. Environ., 284, 113359, https://doi.org/10.1016/j.rse.2022.113359, 2023.

Izeboud, M., Wouters, B., de Roda Husman, S., and Lhermitte, S.: Damage development on Antarctic ice shelves sensitive to climate warming, Nat. Clim. Change, 15, 1333–1339, https://doi.org/10.1038/s41558-025-02453-4, 2025.

Jin, J., Payne, A., and Bull, C.: Current reversal leads to regime change in the Amery Ice Shelf cavity in the 21st century, The Cryosphere, 19, 1873–1896, https://doi.org/10.5194/tc-19-1873-2025, 2025.

Joughin, I., Shapero, D., Smith, B., Dutrieux, P., and Barham, M.: Ice-shelf retreat drives recent Pine Island Glacier speedup, Sci. Adv., 7, eabg3080, https://doi.org/10.1126/sciadv.abg3080, 2021.

King, E. C., De Rydt, J., and Gudmundsson, G. H.: The internal structure of the Brunt Ice Shelf from ice-penetrating radar analysis and implications for ice shelf fracture, The Cryosphere, 12, 3361–3372, https://doi.org/10.5194/tc-12-3361-2018, 2018.

Lai, C., Kingslake, J., Wearing, M., Chen, P., Gentine, P., Li, H., Spergel, J., and van Wessem, J.: Vulnerability of Antarctica's ice shelves to meltwater-driven fracture, Nature, 584, 574–578, https://doi.org/10.1038/s41586-020-2627-8, 2020.

Lhermitte, S., Sun, S., Shuman, C., Wouters, B., Pattyn, F., Wuite, J., Berthier, E., and Nagler, T.: Damage accelerates ice shelf instability and mass loss in Amundsen Sea Embayment, P. Natl. Acad. Sci. USA, 117, 24735–24741, https://doi.org/10.1073/pnas.1912890117, 2020.

Li, G., Guo, J., Pei, L., Zhang, S., Tang, X., and Yao, J.: Extraction and Analysis of the Three-Dimensional Features of Crevasses in the Amery Ice Shelf Based on ICESat-2 ATL06 Data, IEEE J. Select. Top. Appl. Earth Obs. Remote Sens., 14, 5796–5806, https://doi.org/10.1109/jstars.2021.3085302, 2021.

Li, Q., An, J., Xing, Z., Wang, Z., Jiang, P., Yan, B., Wu, Y., and Zhang, B.: Three-dimensional dynamic monitoring of crevasses based on deep learning and surface elevation reconstruction methods, Int. J. Appl. Earth Obs. Geoinf., 132, 104017, https://doi.org/10.1016/j.jag.2024.104017, 2024a.

Li, Q., Wang, Z., An, J., and Zhang, B.: Three-Dimensional Characterization of Pan-Antarctic Ice Shelf Fracture: An Integrated Deep Learning and Hydrological Analysis Framework, IEEE Geosci. Remote Sens. Lett., 22, 1–5, https://doi.org/10.1109/lgrs.2025.3595934, 2025a.

Li, Q., Wang, Z., An, J., Liu, M., Jiang, P., and Shi, Z.: Assessment of Larsen C Ice Shelf stability: insights from surface and basal fracture, Int. J. Digit. Earth, 18, 2475165, https://doi.org/10.1080/17538947.2025.2475165, 2025b.

Li, T., Heidler, K., Mou, L., Ignéczi, A., Zhu, X. X., and Bamber, J.: A high-resolution calving front data product for marine-terminating glaciers in Svalbard, Earth Syst. Sci. Data, 16, 919–939, https://doi.org/10.5194/essd-16-919-2024, 2024b.

Lilien, D., Joughin, I., Smith, B., and Shean, D.: Changes in flow of Crosson and Dotson ice shelves, West Antarctica, in response to elevated melt, The Cryosphere, 12, 1415–1431, https://doi.org/10.5194/tc-12-1415-2018, 2018.

Lv, D., Cheng, Y., Xiao, H., and Hai, G.: A Framework for Fracture Extraction Under Glaciological Property-Based Constraints: Scientific Application on the Filchner-Ronne Ice Shelf of Antarctica, Earth Space Sci., 9, e2022EA002293, https://doi.org/10.1029/2022ea002293, 2022.

Marsh, O., Arthern, R., and De Rydt, J.: Ocean tides trigger ice shelf rift growth and calving, Nat. Commun., 16, 6697, https://doi.org/10.1038/s41467-025-61796-w, 2025.

Massom, R. A., Scambos, T. A., Bennetts, L. G., Reid, P., Squire, V. A., and Stammerjohn, S. E.: Antarctic ice shelf disintegration triggered by sea ice loss and ocean swell, Nature, 558, 383–389, https://doi.org/10.1038/s41586-018-0212-1, 2018.

McGrath, D., Steffen, K., Scambos, T., Rajaram, H., Casassa, G., and Rodriguez Lagos, J. L.: Basal crevasses and associated surface crevassing on the Larsen C ice shelf, Antarctica, and their role in ice-shelf instability, Ann. Glaciol., 53, 10–18, https://doi.org/10.3189/2012AoG60A005, 2012.

Miles, B. W. J. and Bingham, R. G.: Progressive unanchoring of Antarctic ice shelves since 1973, Nature, 626, 785–791, https://doi.org/10.1038/s41586-024-07049-0, 2024.

Miles, B. W. J., Li, T., and Bingham, R.: Totten Ice Shelf history over the past century interpreted from satellite imagery, The Cryosphere, 19, 4027–4043, https://doi.org/10.5194/tc-19-4027-2025, 2025.

Morris, A., Lipovsky, B., Walker, C., and Marsh, O.: Ice shelf calving due to shear stresses: observing the response of Brunt Ice Shelf and Halloween Crack to iceberg calving using ICESat-2 laser altimetry, satellite imagery, and ice flow models, The Cryosphere, 19, 4303–4325, https://doi.org/10.5194/tc-19-4303-2025, 2025.

Mouginot, J., Scheuchl, B., and Rignot, E.: MEaSUREs Antarctic Boundaries for IPY 2007–2009 from Satellite Radar, Version 2, NASA National Snow and Ice Data Center Distributed Active Archive Center [data set], https://doi.org/10.5067/AXE4121732AD, 2017.

Ochwat, N., Scambos, T., Banwell, A., Anderson, R., Maclennan, M., Picard, G., Shates, J., Marinsek, S., Margonari, L., Truffer, M., and Pettit, E.: Triggers of the 2022 Larsen B multi-year landfast sea ice breakout and initial glacier response, The Cryosphere, 18, 1709–1731, https://doi.org/10.5194/tc-18-1709-2024, 2024.

Otosaka, I., Shepherd, A., Ivins, E., Schlegel, N., Amory, C., van den Broeke, M., Horwath, M., Joughin, I., King, M., Krinner, G., Nowicki, S., Payne, A., Rignot, E., Scambos, T., Simon, K., Smith, B., Sorensen, L., Velicogna, I., Whitehouse, P., Geruo, A., Agosta, C., Ahlstrom, A., Blazquez, A., Colgan, W., Engdahl, M., Fettweis, X., Forsberg, R., Gallée, H., Gardner, A., Gilbert, L., Gourmelen, N., Groh, A., Gunter, B., Harig, C., Helm, V., Khan, S., Kittel, C., Konrad, H., Langen, P., Lecavalier, B., Liang, C., Loomis, B., McMillan, M., Melini, D., Mernild, S., Mottram, R., Mouginot, J., Nilsson, J., Noël, B., Pattle, M., Peltier, W., Pie, N., Roca, M., Sasgen, I., Save, H., Seo, K., Scheuchl, B., Schrama, E., Schröder, L., Simonsen, S., Slater, T., Spada, G., Sutterley, T., Vishwakarma, B., van Wessem, J., Wiese, D., van der Wal, W., and Wouters, B.: Mass balance of the Greenland and Antarctic ice sheets from 1992 to 2020, Earth Syst. Sci. Data, 15, 1597–1616, https://doi.org/10.5194/essd-15-1597-2023, 2023.

Pang, A., Liang, Q., Li, W., Zheng, L., Li, T., and Cheng, X.: The distribution and evolution of surface fractures on pan-Antarctic ice shelves, Int. J. Digit. Earth, 16, 3295–3320, https://doi.org/10.1080/17538947.2023.2246436, 2023.

Pang, A., Liang, Q., Hulbe, C., Yang, T., Zhou, Q., Forbes, M., and Cheng, X.: A Framework for Characterizing 3-D Structures of Crevasses and Rifts Across Antarctic Ice Shelves, IEEE T. Geosci. Remote, 64, 4300119, https://doi.org/10.1109/tgrs.2025.3645189, 2026.

Qiao, G., Li, Y., Guo, S., and Ye, W.: Evolving Instability of the Scar Inlet Ice Shelf based on Sequential Landsat Images Spanning 2005–2018, Remote Sens., 12, 36, https://doi.org/10.3390/rs12010036, 2020.

Ranganathan, M., Robel, A. A., Huth, A., and Duddu, R.: Glacier damage evolution over ice flow timescales, The Cryosphere, 19, 1599–1619, https://doi.org/10.5194/tc-19-1599-2025, 2025.

Rignot, E., Mouginot, J., and Scheuchl, B.: MEaSUREs InSAR-Based Antarctica Ice Velocity Map, Version 2, NASA National Snow and Ice Data Center Distributed Active Archive Center [data set], https://doi.org/10.5067/D7GK8F5J8M8R, 2017.

Ronneberger, O., Fischer, P., and Brox, T.: U-Net: Convolutional networks for biomedical image segmentation, in: Medical Image Computing and Computer-Assisted Intervention (MICCAI) 2015, 234–241, https://doi.org/10.1007/978-3-319-24574-4_28, 2015.

Scambos, T. A., Haran, T. M., Fahnestock, M. A., Painter, T. H., and Bohlander, J.: MODIS-based Mosaic of Antarctica (MOA) data sets: Continent-wide surface morphology and snow grain size, Remote Sens. Environ., 111, 242–257, https://doi.org/10.1016/j.rse.2006.12.020, 2007.

Spergel, J., Kingslake, J., Creyts, T., van Wessem, M., and Fricker, H.: Surface meltwater drainage and ponding on Amery Ice Shelf, East Antarctica, 1973–2019, J. Glaciol., 67, 985–998, https://doi.org/10.1017/jog.2021.46, 2021.

Studinger, M.: IceBridge ATM L1B Elevation and Return Strength, Version 2, NASA National Snow and Ice Data Center Distributed Active Archive Center [data set], https://doi.org/10.5067/19SIM5TXKPGT, 2013.

Studinger, M. and Harbeck, J.: IceBridge CAMBOT L1B Geolocated Images, Version 2, NASA National Snow and Ice Data Center Distributed Active Archive Center [data set], https://doi.org/10.5067/B0HL940D452L, 2019.

Surawy-Stepney, T., Hogg, A., Cornford, S., and Davison, B.: Episodic dynamic change linked to damage on the Thwaites Glacier ice tongue, Nat. Geosci., 16, 37–43, https://doi.org/10.1038/s41561-022-01097-9, 2023a.

Surawy-Stepney, T., Hogg, A., Cornford, S., and Hogg, D.: Mapping Antarctic crevasses and their evolution with deep learning applied to satellite radar imagery, The Cryosphere, 17, 4421–4445, https://doi.org/10.5194/tc-17-4421-2023, 2023b.

Surawy-Stepney, T., Hogg, A., Cornford, S., Wallis, B., Davison, B., Selley, H., Slater, R., Lie, E., Jakob, L., Ridout, A., Gourmelen, N., Freer, B., Wilson, S., and Shepherd, A.: The effect of landfast sea ice buttressing on ice dynamic speedup in the Larsen B embayment, Antarctica, The Cryosphere, 18, 977–993, https://doi.org/10.5194/tc-18-977-2024, 2024.

Tang, L.: Surface Damage Mapping and Analysis Code (Version v1.0.0) [Computer software], Zenodo [code], https://doi.org/10.5281/zenodo.24334784, 2026a (code also available at: https://github.com/tly-code/surface-damage-seg, last access: 18 November 2026).

Tang, L.: DiffGF Code (Version v1.0.0) [Computer software], Zenodo [code], https://doi.org/10.5281/zenodo.24334780, 2026b (code also available at: https://github.com/tly-code/DiffGF, last access: 18 November 2026).

Tang, L., Bamber, J., Li, T., and Qiao, G.: Surface Damage Dataset for Antarctic Ice Shelves 1999–2024, Zenodo [data set], https://doi.org/10.5281/zenodo.20425951, 2026a.

Tang, L., Bamber, J. L., Qiao, G., and Kong, Y.: A Non-Reference Diffusion-Based Restoration Framework for Landsat 7 ETM+ SLC-off Imagery in Antarctica, IEEE J. Select. Top. Appl. Earth Obs. Remote Sens., 19, 30257–30274, https://doi.org/10.1109/JSTARS.2026.3720971, 2026b.

Walker, C., Becker, M., and Fricker, H.: A High Resolution, Three-Dimensional View of the D-28 Calving Event From Amery Ice Shelf With ICESat-2 and Satellite Imagery, Geophys. Res. Lett., 48, e2020GL091200, https://doi.org/10.1029/2020gl091200, 2021.

Wang, S., Alexander, P., Wu, Q., Tedesco, M., and Shu, S.: Characterization of ice shelf fracture features using ICESat-2-A case study over the Amery Ice Shelf, Remote Sens. Environ., 255, 112266, https://doi.org/10.1016/j.rse.2020.112266, 2021.

Wang, S., Alexander, P., Alley, R., Huang, Z., Parizek, B., Willet, A., and Anandakrishnan, S.: Recent Variability in Fracture Characteristics and Ice Flow of Thwaites Ice Shelf, West Antarctica, J. Geophys. Res.-Earth, 130, e2024JF008118, https://doi.org/10.1029/2024jf008118, 2025.

Wang, Z. and Bovik, A.: A universal image quality index, IEEE Signal Proc. Lett., 9, 81–84, https://doi.org/10.1109/97.995823, 2002.

Wang, Z., Bovik, A., Sheikh, H., and Simoncelli, E.: Image quality assessment: From error visibility to structural similarity, IEEE T. Image Process., 13, 600–612, https://doi.org/10.1109/tip.2003.819861, 2004.

Xie, E., Wang, W., Yu, Z., Anandkumar, A., Alvarez, J. M., and Luo, P.: SegFormer: Simple and Efficient Design for Semantic Segmentation with Transformers, Adv. Neural Inf. Process. Syst., 34, 12077–12090, 2021.

Xu, B., Liang, Q., Chang, B., Li, Y., Li, T., Zheng, L., Zhang, W., and Cheng, X.: Extracting Antarctic ice shelf fracture depths using the linear cloth simulation filtering al-

gorithm, Int. J. Appl. Earth Obs. Geoinf., 149, 105255, https://doi.org/10.1016/j.jag.2026.105255, 2026.

Zhang, R., Isola, P., Efros, A., Shechtman, E., and Wang, O.: The Unreasonable Effectiveness of Deep Features as a Perceptual Metric, in: 31st IEEE/CVF Conference on Computer Vision and Pattern Recognition (CVPR), 586–595, https://doi.org/10.1109/cvpr.2018.00068, 2018.

Zhao, J., Liang, S., Li, X., Duan, Y., and Liang, L.: Detection of Surface Crevasses over Antarctic Ice Shelves Using SAR Imagery and Deep Learning Method, Remote Sens., 14, 487, https://doi.org/10.3390/rs14030487, 2022.

Zheng, K., Li, Q., Wang, Z., An, J., Huang, F., Liu, M., and Bao, S.: CREVNet: A Transformer and CNN-Based Network for Accurate Segmentation of Ice Shelf Crevasses, IEEE Geosci. Remote Sens. Lett., 21, 1–5, https://doi.org/10.1109/lgrs.2024.3407860, 2024.

Zhu, Q., Guo, H., Zhang, L., Liang, D., Wu, Z., Liu, Y., and Lv, Z.: GLA-STDeepLab: SAR Enhancing Glacier and Ice Shelf Front Detection Using Swin-TransDeepLab With Global-Local Attention, IEEE T. Geosci. Remote, 61, 5218113, https://doi.org/10.1109/tgrs.2023.3324404, 2023.